Corrosion resistance of functionally graded TiN/Ti coatings for proton exchange membrane fuel cells

Preprint *in* International Journal of Hydrogen Energy · October 2020

DOI: 10.1016/j.ijhydene.2020.09.037

7 authors, including:

Oscar Prada
University of São Paulo
5 PUBLICATIONS **20** CITATIONS
SEE PROFILE

Julio César Sagás
Universidade do Estado de Santa Catarina
46 PUBLICATIONS **259** CITATIONS
SEE PROFILE

Cláudio Geraldo Schön
University of São Paulo
147 PUBLICATIONS **985** CITATIONS
SEE PROFILE

Luis C Fontana
Universidade do Estado de Santa Catarina
63 PUBLICATIONS **305** CITATIONS
SEE PROFILE

Corrosion resistance of functionally graded TiN/Ti coatings for proton exchange membrane fuel cells

F.C. Silva[a,b,*], O.M.Prada Ramirez[a], M.A. Tunes[c], P.D. Edmondson[d], J.C. Sagás[e], L.C. Fontana[e], H.G. de Melo[a], C.G. Schön[a]

[a]*Departamento de Engenharia Metalúrgica e de Materiais, Escola Politécnica da Universidade de São Paulo, Av. Prof. Mello Moraes, 2463, 05508-900 São Paulo-SP, Brazil.*
[b]*Faculdade de Tecnologia de Cotia, Centro Estadual de Educação Tecnológica "Paula Souza", Rua Nelson Raineri, 700, 06702-155 Cotia – SP, Brazil.*
[c]*Chair of Non-Ferrous Metallurgy, Montanuniversitaet Leoben, Franz-Josef-Strasse 18, 8700 Leoben, Austria*
[d]*Materials Science and Technology Division, Oak Ridge National Laboratory, 1 Bethel Valley Rd, Oak Ridge, TN 37830, United States of America.*
[e]*Laboratory of Plasmas, Films and Surfaces, Universidade do Estado de Santa Catarina, Rua Paulo Malschitzki, 200 – Zona Industrial Norte, 89219-710, Joinville-SC, Brazil.*

Abstract

Bipolar Plates (BPP) are important components of proton exchange membrane fuel cell (PEMFC) stacks. In the development of innovative fuel cell designs, it is advantageous to use aluminum for these applications, however, this material lacks the necessary corrosion resistance. Since the performance of PEMFC stacks depends on BPP properties, in particular, corrosion resistance, depositing titanium nitride (TiN) thin films onto aluminum substrates may improve their efficiency and durability. Present work focuses on improving corrosion resistance and hydrophobicity of TiN/Ti by using N graded films deposited onto aluminum substrates (AA-1100) by grid-assisted magnetron sputtering (GAMS). Electrochemical impedance spectroscopy (EIS) with potentiodynamic and potentiostatic polarization are used to investigate the performance of the substrate/film system at room temperature and 70 ^{o}C, thus simulating a prototypic PEMFC electrolyte environment. Electrochemical test results showed that graded TiN films improved corrosion resistance when compared with both the homogeneous films and the AA1100 uncoated substrate. Furthermore, contact angle results reveal improved hydrophobicity for both homogeneous and graded TiN coatings when compared with the AA1100 substrate.

Keywords: PEMFC, Titanium Nitride, Bipolar Plates, Graded Coatings, Functionally Graded Materials, Corrosion Resistance

1. Introduction

Development of modern society and energy generation are intrinsically associated [1]. Even considering that fossil fuel has prevailed in the last two centuries [2], concerns about decreasing greenhouse gases

*Corresponding author: Tel. +55-11-996170027.
Email address: felipecarneiro@usp.br (F.C. Silva)

(GHG) emissions, such as CO_2, led to the increased participation of clean energy sources in the global energy matrix [3–6].

Fuel cell (FC) technology is an efficient and environmentally sustainable solution compared with other environmentally friendly alternatives [7]. They consist of devices designed to convert chemical energy to electricity by means of electrochemical reactions involving hydrogen and oxygen [8]. Among the existing fuel cell designs, proton-exchange membrane fuel cell (PEMFC) stacks currently dominate both research and the market and they have been considered as sustainable energy solutions for future substitution of internal combustion engines applications [9, 10]. They operate at relatively low temperatures (70-90^{o}C) combined with small dimensions, fast start-up responses, almost zero carbon-based gases emission, high energy efficiency, and low noise and vibration levels [11–13].

Considered the backbone of PEMFCs [14–17], the bipolar plates (BPP) are responsible for 18-37% of the fuel cell price, most of the mass (about 80%) and 70% of the cell volume [17–20]. To increase the power delivery, PEMFCs are combined in stacks which are held together under a certain applied load. Improvement of the BPPs is an industry requirement and it has a large potential for the further development of these fuel cells.

The performance of PEMFC stacks is highly dependent on the properties of BPPs [18]. Graphite is the most common material currently applied to produce BPPs. It has good corrosion resistance and chemical stability in the aggressive PEMFC environment, high electrical conductivity and high mechanical strength [21–23]. This material, however, displays several disadvantages such as heavy weight (due to the large volume needed), expensive manufacturing costs, inherent porosity and brittleness [17, 24–26]. The latter disadvantage is particularly inappropriate for using in automotive engines as the devices will be constantly submitted to shocks and vibrations in service [27]. Moreover, brittleness is also a drawback if we consider that the PEMFC stacks are assembled under high compressive load.

Recently, metallic plates have been tested to substitute graphite in BPPs [28–30]. Metallic plates exhibit better mechanical strength, higher electrical conductivity, lower manufacturing cost and weight (as they can be produced in smaller volumes) and better gas permeability compared with graphite [31–34]. Metallic BPPs are, however, vulnerable to corrosion in the acid harsh environment of PEMFCs, limiting their performance. Two major drawbacks are herein identified: (i) the formation of either insulating surface corrosion products or oxide layer build up, increasing the interface contact resistance (ICR) [19, 27, 35], and (ii) the "poisoning" of the membrane by the metallic cations, leading to a decrease of the power output with time [19]. According to several authors this latter issue would be linked to the displacement of H^+ ions from the membrane by the multivalent metal cations, which present higher affinity for the sulfonic groups of the

electrolyte [36, 37].

Application of corrosion resistant and electron conducting coatings to metallic substrates is a possible solution to improve the performance of prototypic metallic BPPs. This approach is fundamentally different from that used in classical corrosion protection procedures in which insulating coatings are commonly used. Several alternatives have been proposed, some examples are herein summarized:

- Semiconducting polymer coatings [38–40];
- Ceramic coatings like
  - chromium nitride (CrN) [41–43];
  - titanium nitride (TiN) [41, 44];
  - chromium carbide (CrC) [42];
  - multilayered coatings [30];
  - ternary nitride coatings [41];
- Implantation of noble metals [45] and
- Carbon-based coatings [17, 46].

These authors often report an improvement of the corrosion behavior of the coated BPP when compared to the bare metal, indicating that this approach could be effective to control the corrosion resistance.

Concerning the metallic substrate, the majority of works were performed using stainless steels, as documented in recent reviews by Antunes *et al.*, Taherian *et al.* and Leng *et al.* [19, 46, 47]. However, considering important requirements for PEMFC for automotive applications, like weight and electric conductivity, aluminum outperforms stainless steel as it is less dense and presents better electrical conductivity. For instance, Lee *et al.* [8] reported a 63% weight reduction for a PEMFC stack when changing the BPP material from stainless steel to aluminum. These authors also mention that the resistivity of stainless steel is 27 times higher than aluminum.

For example, Joseph *et al.* [38] reported results obtained by applying the conductive polymers polypyrrole (PPY) and polyaniline (PANI) to AA-6061 BPPs. These authors observed a lower corrosion current density (i_{corr}) for the plates protected with PANI, compared with the plates protected with PPY. This was ascribed to the presence of pinholes in the coating, which were associated to the activation procedure used prior to PPY deposition. This shows that the growth mechanism of the films may have a severe impact on the performance of the protective coating.

Among the tested coatings to protect BPPs, TiN seems to be one of the most promising solutions due to its high hardness, excellent corrosion resistance and good chemical stability in acidic electrolytes [48, 49]. In addition it possess suitable thermal stability due to its high melting point [50, 51] and an electronic structure similar to noble metals, thus behaving as such in electrolytes [48]. TiN coatings also present smaller interface contact resistance compared with metals protected by their naturally formed oxide layers [8], and shows an electrical conductivity about one order of magnitude higher than graphite (about 4.5 x 10^6 S.m^{-1} compared with 1.0 x 10^5 S.m^{-1} for graphite) [46, 49]. These coatings have already been successfully applied in many branches of the industry, for improving surface properties in mechanical tools, metal forming, aerospace engineering, automotive, microelectronics and biomedical applications [52–58]. This shows that there is a large knowledge basis about these coating collected for different applications.

In the literature, several studies are available where TiN coatings were used to protect metallic substrates aimed for BPP application [34, 59–61]. Corrosion resistance studies of TiN films deposited on AISI 316L substrates both at room temperature and in PEMFC simulated environments are reported by several authors [59, 60, 62]. The results show, in general, that the coating improved the corrosion resistance of the substrate in both conditions, and as a bonus, they increase the hydrophobicity of the surface. The authors justify these result due to the homogeneous, compact and dense films which are obtained, leading to improved adhesion.

TiN coatings were also deposited on Ti and Al [8, 34] substrates and tested under operating PEMFC environments. In both cases the coated samples were reported to present higher corrosion resistance and lower interface contact resistance compared with the unprotected substrates. Lee *et al.* [8] investigated multilayer coatings of TiO_2/Ti and TiN/Ti, applied on Al 6061 substrate. The corrosion behavior was tested in the cathodic and anodic PEMFC environments. The Ti interlayer was applied in contact with the substrate for reducing mechanical and thermal impact characteristics of fuel cells manufacturing and operation. For both conditions, and for the two coatings, a reduction of the i_{corr} of more than one order of magnitude was verified when compared to the unprotected metal; moreover, the i_{corr} of the coated samples determined by the Tafel extrapolation methodology were close to the 1.0 μA.cm $^{-2}$ threshold, established by the United States Department of Energy (US DOE) [63] as a criterion for producing fuel cells. Regarding the comparative behavior of the two coatings, Lee *et al.* [8] report slightly lower i_{corr} for the Ti/TiO_2 coating, which, nevertheless, showed much higher ICR and lower conductivity, leading the authors to suggest that the TiN/Ti coating was more adequate for PEMFC use.

Li *et al.* [64] studied the corrosion behavior of AA5052 BPPs protected with monolayer (TiN, CrN, C) and bilayer (C/TiN and C/CrN) coatings applied by close field unbalanced magnetron-sputter ion plating, testing them in both anodic and cathodic PEMFC environments. The authors reported that in all cases

an improved corrosion resistance was observed when compared with the bare substrate. In general, the C/CrN coatings presented the better performance, however, in the cathodic environment all the coatings presented i_{corr} values more than one order of magnitude superior to the threshold established by the US DOE [64]. Specifically regarding the TiN coatings, the monolayer presented a more active performance due to the presence of pinholes in the film. This drawback could be overcome by using the bi-layer system, which showed i_{corr}, respectively, two and one order of magnitude smaller than the corresponding monolayer versions in the anodic and in the cathodic environment. These authors also report the use of a thin (100 nm) metallic (Ti or Cr) seed layer to enhance adhesion of the layers with the substrate [64].

TiN coatings produced by magnetron sputtering have good uniformity and increased corrosion resistance [60]. TiN film properties can be modified controlling the atomic N/Ti flux ratio [65, 66]. Therefore, the increase in N_2 flow rate during reactive TiN deposition can be used to change the structure, composition and preferred orientation of the films, producing N graded films [58, 67]. Such strategy can improve bio-compatibility, wear resistance[58] and mechanical properties[68] of the films.

In a recent work, some of the authors of the present study grown TiN films with a nitrogen gradient along film thickness on AA1010 substrates through grid-assisted magnetron sputtering (GAMS) [67]. These films exhibited characteristics which make them distinct from usual homogeneous TiN sputtered films, like a change in the preferred grain orientation of the film, which could potentially lead to improved corrosion resistance in the acidic environments typical of PEMFC.

In the present work, homogeneous and graded TiN/Ti coatings deposited over AA1100 substrates via GAMS are investigated concerning their corrosion resistance and hydrophobicity. The performance of the coated substrates was evaluated in emulated cathodic environments characteristic of PEMFCs both at room temperature and at 70 ^{o}C. Some insights about the film structure are also presented.

2. Methodology

2.1. Materials preparation and synthesis

A commercially pure aluminium sheet (AA1100) was used in the investigation. The samples were initially ground with SiC grinding paper down to grit 2000 and subsequently polished using 1 μm diamond paste in NAP cloth. Then, they were thoroughly washed with distilled water and ethanol and dried with a hot air stream. Prior to deposition, the specimens were ultrasonically cleaned in tetrachloroethylene for 10 minutes. Homogeneous and graded TiN/Ti bilayer coatings, hereafter denominated TiN coatings for the sake of simplicity, were deposited onto AA1100 substrates by GAMS technique [67]. Titanium sputtering target (99.5% pure) has a thickness of 5 mm and a diameter of 100 mm. The austenitic stainless steel grid

(mesh 1 × 1 mm) was kept grounded, being the main discharge anode. The target-to-grid distance was 20 mm, while the target-to-substrate distance was 60 mm. The total pressure was fixed at 0.40 Pa, and the discharge current at 2.00 A. The substrate was heated to 300 ^{o}C. Before the TiN film deposition, a Ti interlayer (about 150 nm) was deposited in a pure Ar (99.999%) discharge to improve film adhesion (as suggested by previous works[64, 69–71]). Then, N_2 (99.999%) was inserted into the chamber to deposit TiN, maintaining the other deposition conditions.

The N_2 flow rate was fixed at 8.0 sccm for the homogeneous TiN coatings. Conversely, for the graded TiN coatings, the N_2 flow rate was set initially to 1.5 sccm and then the flow rate was increased in steps of 0.4 sccm min^{-1} up to around 8.0 sccm; therefore, the nitrogen content increases from the bottom to the top of the coating. For the last deposition time, the N_2 flow rate was maintained constant. Independently of the N_2 flow conditions, the deposition rate was around 65 nm min^{-1}, and the total deposition time was set to 30 min. The DC substrate bias was set to -40 V for all N_2 flow conditions. According to X-Ray Photoelectron Spectroscopy (XPS) measurements, both homogeneous and graded films show (besides adventitious carbon) an oxygen surface contamination due to exposure to air. The O/Ti ratio at the surface is 0.73 for the homogeneous film and 0.54 for the graded film. The oxygen is only at the surface, being removed after 240 s of sputter cleaning with an Ar ion gun. More details about the deposition procedure and XPS measurements are described elsewhere [67].

2.2. Contact angle measurements

The sessile drop method was used to evaluate the wettability of the aluminum substrate and the TiN coated samples by measuring the static contact angle (θ) with distilled water. The experiments were carried out with a Dataphysics Contact angle System OCA, using a digital analysis software (Dataphysics SCA 20). A high resolution digital camera provided with the equipment was used to analyze the recorded image. Before the measurements, which were performed at least three times, the specimens were thoroughly washed with distilled water and ethanol and dried with a hot air stream.

2.3. Electrochemical measurements

A Potentiostat/Galvanostat/ZRA Gamry reference 600+ was used for the eletrochemical tests. A three-electrode cell comprising the aluminum sample, without or with the different TiN films, as working electrode, an Ag/AgCl reference electrode and a platinum wire counter electrode was applied for the electrochemical tests in this work. The measurements were carried out in a solution of 0.5M H_2SO_4 with 2 ppm HF at both 25 ^{o}C, referred as room temperature (RT) condition, and 70 ^{o}C both of them with oxygen saturation. This latter condition aims to simulate the PEMFC cathode environment[62].

All tests were carried out with a microcell with 15 ml electrolyte volume at which the working electrode exposed area was approximately 0.283 cm^2. In order to verify reproducibility, all the measurements presented in this work were performed at least three times.

The potentiodynamic polarization tests were carried out after 30 minutes stabilization of the open circuit potential (OCP) in the range from -0.2 V vs. OCP to +1.5 V vs. OCP at a scan rate of 1 mV S^{-1}. Gamry Echem Analyst software was employed for determining the corrosion potential (Ecorr) and the corrosion current density (i_{corr}), from the extrapolation of the cathodic branch of the curves.

Potentiostatic measurements were conducted at +0.6 V vs. Ag/AgCl for 1 h, corresponding to the operating potential of the PEMFC cathode [62]. The polarization procedure was started after 30 minutes stabilization of the OCP. For the electrochemical impedance spectroscopy (EIS) experiments, the frequency range was from 10^5 to 10^{-2} Hz, and the alternate current (ac) signal was set to 15 mV (rms), with an acquisition rate of seven points per decade. The diagrams were acquired at the OCP after stabilization for 1h.

2.4. Transmission Electron Microscopy (TEM)

Prior to electron-microscopy, electron-transparent samples of both homogeneous and graded TiN thin films were obtained with conventional TEM lift-out procedure in a focused ion beam (FIB) [72]. Two electron-microscopes were used in this work to obtain microstructural images of both homogeneous and graded TiN films: a Hitachi H9500 operating with a LaB_6 filament at 300 keV and a JEOL JEM 2100F operating with a field emission gun at 200 keV. The electron-microscopy investigation shown in this present work was carried out using bright-field TEM (BFTEM). Detailed information regarding the microstructure of both TiN films was already published elsewhere [67].

2.5. Electron Energy Loss Spectroscopy (EELS)

Prior to analytical electron-microscopy with EELS, electron-transparent lamellae were produced from bulk graded TiN films deposited on aluminum substrate using conventional Focused-Ion Beam (FIB) lift-out technique for TEM samples [73]. Prior the milling stage, a 3.0 μm top-layer of Pt was deposited on the TiN surface in order to avoid FIB damage. EELS characterization of the graded TiN film was performed in a JEOL JEM 2100F TEM operating at 200 keV with a Schottky Field Emission Gun (FEG) located at the Low-Activation Materials Development and Analysis (LAMDA) laboratory at the Oak Ridge National Laboratory. The TEM is equipped with a Gatan 963 GIF Quantum Electron Energy Loss Spectrometer with nominal energy resolution of 0.9 eV. During the EELS acquisition, the maximum achieved energy resolution, assessed by the full width at half maximum of the Zero-Loss Peak (ZLP), was within the range

of 0.8 – 1.0 eV using a 5 mm aperture after appropriate electron beam alignment. Each EELS spectrum represents an average of 10 collected curves for each analyzed region.

3. Results and discussion

3.1. Contact angle measurements

Figure 1 shows the contact angles for the uncoated substrate and for samples coated with both films (homogeneous and graded TiN). The uncoated substrate exhibits a smaller contact angle (about 60^{o}) when compared with both coated samples (about 90^{o}), showing that TiN coated BPP has increased hydrophobicity, independently on the film growth mode.

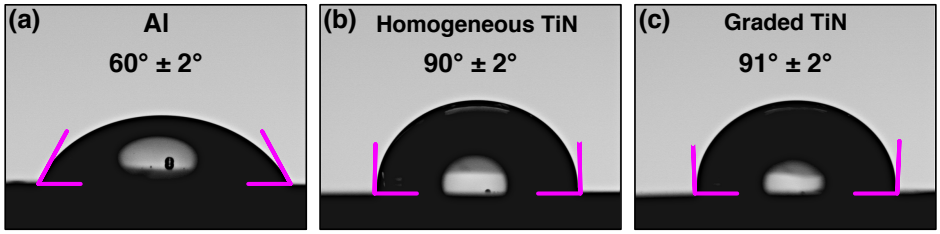

Figure 1: Water contact angle measurements in the (a) uncoated substrate, (b) homogeneous TiN film and (c) graded TiN film on aluminum substrates.

Water interaction is listed among the key factors that can affect the performance of a fuel cell. In a PEMFC cathode side, water is generated as a by-product of the electrochemical reactions, and is also introduced in the cell via the previous humidification of incoming gases aiming increased hydration of the MEA, thus improving its proton conductivity [74]. According to the literature, the flooding of the BPP flow channels due to water accumulation hinders the access of the reactant gases to the active electrodes sites, isolates the catalyst due to submersion and, in addition, accelerates the BPP corrosion due to emission of F^{-} ions from the membrane [35, 62, 74]. Therefore, the smaller the surface wettability (larger hydrophobicity) of the BPP, the easier it is for the water to be removed from the PEMFC stack, improving the performance of the cell [75]. This property can be evaluated by determining the water contact angle, where the higher the contact angle the more hydrophobic the surface. Among the factors that can influence surface wettability in can be listed chemical properties, surface energy and planes orientations [62, 76].

In a recent investigation, Jannat *et al.* [62] also reported an increase in the contact angle of about 30^{o} for a Ti/TiN coated stainless steel sample when compared to the uncoated metal, the authors described this difference to the increased electronegativity of the air-formed chromium oxide layer when compared to the TiN coating, as the highly electronegative oxygen would display increased affinity to the water molecules. This can also apply to explain the results found in the present investigation, as Al is also protected by a

naturally formed oxide (passivation) layer. Finally, it is important to emphasize that the similarity between the contact angles of the coated samples was an expected outcome as, for the graded coating, the N content increases from the bottom to the top; therefore, the surface N content, i.e. the chemical composition, is similar for both coatings. Despite the XPS results show high oxygen content at the TiN surface for the films, both graded and homogeneous, its surface remain hydrophobic since the contact angle is approximately 90^0. The oxygen on the TiN surface works differently from the native oxide layer on the Ti metal surface. The results of XPS also show that all oxygen is removed after cleaning the surface with Argon, thus this oxyde layer must very thin and similar for both materials.

3.2. Electrochemical measurements

3.2.1. Potentiodynamic polarization

Figure 2 presents the potentiodynamic polarization curves of the aluminum samples, with and without the TiN coatings, as determined in the 0.5 M H_2SO_4 with 2 ppm HF solution at RT (a) and at 70 ^oC (b). The dashed lines indicate the response at +0.6 V vs. Ag/AgCl, close to the typical cathode potential at the PEMFC operating condition [60]. Independent of the solution temperature, the polarization curves present a similar shape, with the cathodic branch showing an activation-controlled process, and the anodic branch exhibiting a current plateau with quasi-stationary current density, indicating a passive behavior. For all conditions, the cathodic process can be described by the oxygen reduction reaction (ORR) in acidic conditions where the typical diffusion-controlled process is not evidenced due to the excess O_2 in the electrolyte.

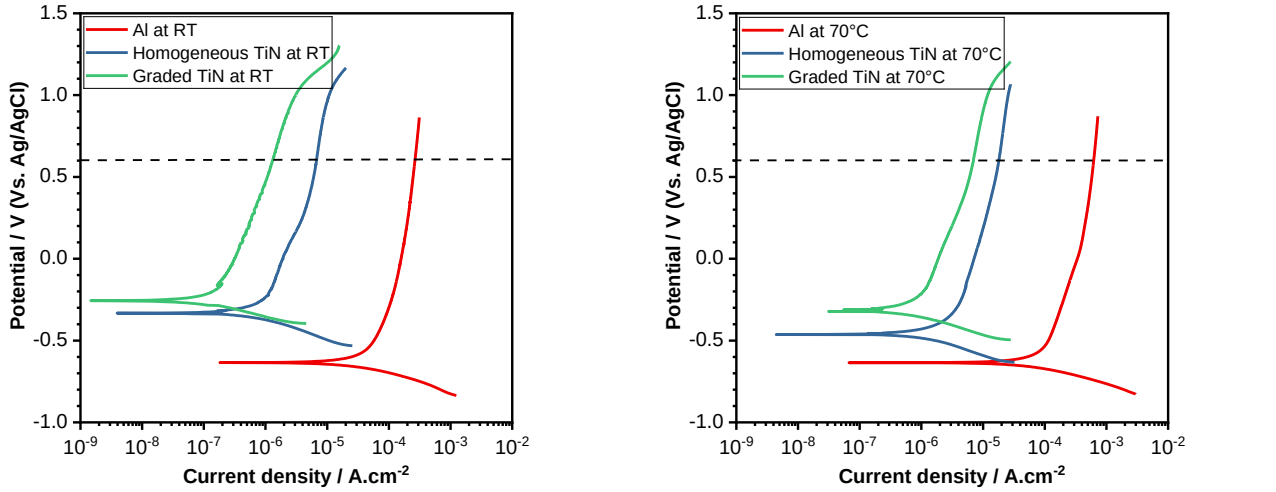

(a) (b)

Figure 2: Potentiodynamic polarization curves for Al 1100, uncoated and coated with homogeneous and graded TiN coating in O_2 saturated 0.5M H_2SO_4 + 2 ppm HF solution at a) 25 ^oC b) 70 ^oC. Scan rate 1 mV S^{-1}

The anodic responses depicted in Figure 2 must be analyzed taking into account both the values of the current densities in the plateau and the solution volume in the electrochemical cell (15 ml), which may

lead to important changes in the solution chemistry near the electrode surface when the dissolution rate is high. For the two coated substrates the current densities at the plateau are typical of the passive state, mostly smaller and close to 10^{-6} A.cm^{-2} at RT and below 10^{-5} A.cm^{-2} at 70°C, showing low dissolution rates of the working electrodes. On the other hand, for the uncoated substrates, the current densities are larger than 10^{-4} A.cm^{-2}, which cannot be associated to a passive state. For these samples, the extensive dissolution in both solutions may lead to accumulation of aluminum cations near the electrode/electrolyte interface, resulting in a limiting current density due to concentration polarization. Indeed, at the end of the experiments, the observation of the uncoated samples surfaces showed generalized corrosion, which was an expected outcome due to the low stability of the aluminum oxide layer in acidic environments [77], whereas, no evident sign of corrosion was observed for the coated samples. Therefore, the current plateau with relatively large current densities for the uncoated samples may be associated to diffusion control of Al cations away from the working electrode surface. Indeed, as stressed by different authors [78, 79], one of the main drawbacks associated with the use of cells with limited solution volumes (microcells) to investigate corrosion phenomena is the fact that the transportation of species may be affected by the low volume and by the cell geometry. However, as for the two coated samples the anodic current densities are very small, indicating low dissolution rates, concentration of aluminum cations at the electrode/electrolyte interface can be ruled out as the cause of the quasi-constant current density, and a limited dissolution rate due to the presence of the coatings can be assumed.

The anodic branches of the polarization curves depicted in Figure 2 clearly show that the coated samples present reduced corrosion rates, especially those protected with the graded film. Considering the responses at the potential of +0.6 V vs. Ag/AgCl, the anodic current densities of the graded TiN, the homogeneous TiN and of the uncoated AA1100 were, respectively, 1.31 x 10^{-6} A.cm^{-2}, 6.70 x 10^{-6} A.cm^{-2} and 2.65 $\times$ 10^{-4} A.cm^{-2} at RT and 6.98 $\times$ 10^{-6} A.cm^{-2}, 18.0 $\times$ 10^{-6} A.cm^{-2} and 6.21 $\times$ 10^{-4} A.cm^{-2} at 70 °C (Table 1). In other words, the corrosion rate of the graded TiN coating is about two orders of magnitude smaller when compared with the uncoated sample , and about 4 times smaller when compared with the homogeneous film. Note that these values may be underestimated due to possible concentration polarization process for the uncoated samples, as discussed previously. Finally, for each type of working electrode the anodic current increased with the electrolyte temperature. This is a common feature in the corrosion behavior of metallic BPPs, and is associated with enhanced kinetics of the electrochemical reactions as well as of the diffusion processes with increased temperature, as stressed in other works [32, 62].

Although the cathodic overpotential was only 200 mV, an evident linear region with more than one logarithm decade can be identified for all the polarization curves in Figure 2. Therefore, Tafel extrapolation

Table 1: Electrochemical parameters extracted from the potentiodynamic polarization curves of the samples with and without TiN coatings at RT and a 70 °C with oxygen saturation.

	Potentiodynamic polarization			Potentiostatic polarization
Condition	E_{corr} V vs Ag/AgCl	i_{corr} μA.cm^{-2}	i at +0.6V(Ag/AgCl) μA.cm^{-2}	i at +0.6V(Ag/AgCl) after 1h μA.cm^{-2}
Al RT	- 0.635	48.3	265	78.71
Al 70 °C	-0.635	51.5	621	78.90
Homogeneous TiN RT	-0.333	0.79	6.7	3.51
Homogeneous TiN 70 °C	-0.463	0.93	18	5.91
Graded TiN RT	-0.256	0.075	1.31	0.56
Graded TiN 70 °C	-0.323	0.37	6.98	1.43

of the cathodic branch was performed to determine the corrosion current density (i_{corr}). The values are displayed in Table 1. For the coated samples, the determined i_{corr} indicates decreasing corrosion resistance in the following order: graded TiN RT > graded TiN 70 °C > homogeneous TiN RT > homogeneous TiN 70 °C. In addition, all the extrapolated values were smaller than 1 μA.cm^{-2}, established by the US DOE as the threshold for BPP application.

The data displayed in Table 1 also show that the ratios between i_{corr} for the uncoated aluminum and for the sample coated with the homogeneous TiN layer were 61.5 and 55.5 for the tests performed at RT and 70 °C, respectively, whereas considering the graded TiN coating the ratios were 644 and 139, confirming the improved performance of this latter coating. These ratios are larger than those determined at +0.6 V Ag/AgCl, further indicating that at high anodic overpotentials, when the dissolution rate increases, the anodic process may be diffusion-controlled for the uncoated samples. This statement is based on the assumption that it should not be expected that the increase of the current density of the unprotected sample for larger overpotentials would be smaller than that verified for the protected ones.

Finally, the polarization curves of Figure 2 show that the cathodic slopes are quite similar. Therefore, the increased corrosion potential (E_{corr}) sequence: graded TiN > homogeneous TiN > uncoated sample, can be associated to the polarization of the anodic reaction, indicating that the coatings protected the substrates surfaces from corrosion by blocking the metallic oxidation. As evidenced in all the results, this process was more efficient for the graded TiN film coating.

The investigation of the applied potential influence on the corrosion resistance of BPPs is often complemented by the presentation of potentiostatic polarization curves acquired at the typical working potential of the PEMFC [8, 62]. The procedure aims simulating the stability of the plates close to a real in-service condition.

The results of the potentiostatic polarization experiments of the aluminum samples, with and without the TiN coatings, at +0.6 V vs. Ag/AgCl at RT and at 70 °C, are plotted in Figure 3, the responses were

tracked along 3600 s. Figures 3a and 3b show that, independently of the BPP condition, there is a current peak followed by transient which decreases exponentially for longer times. This phenomenon is associated with the charging of the interface after the potential step and is mostly composed of a large non-Faradaic component. The current decaying time depends on the system's time constant [80]. The faster decay rate observed for the TiN coated samples (Figure 3b) indicates a faster charging of the interface (smaller time constant) and a smaller contribution of the Faradaic processes to the overall current. Interestingly, the shape of the current transient of the uncoated samples (Figure 3a) is different from the coated ones, specially that obtained at 70 ^{o}C. For these cases, after the exponential decay, the current goes through a minimum, increases again, and then decreases and stabilizes in a constant level (plateau). This sequence is similar to what is found on porous anodizing procedure of aluminum. The initial exponential decay is governed by the thickening of the barrier oxide layer. On the other hand, the current minimum is associated with pore initiation [81]. At this point, according to the literature, the current becomes concentrated in certain regions of the barrier layer either associated with local imperfections [82] or with cracks developed due to accumulated tensile stress [83]. This leads to the local thinning of the barrier layer, explaining the subsequent tiny maximum [84, 85]. The subsequent current decay has been attributed to a decrease in the pores' density, ascribed both to the merging of embryopores into dominant ones and to the dying of embryopores that do not succeed to growth [86]. Finally, the current plateau characterizes the pore development at the base of the major pores [85]. It is important to emphasize that one of the main industrial procedures used to produce porous aluminum oxide layer employs sulfuric acid as electrolyte, clearly the conditions used in the present work are not ideal and, therefore, high current densities are found for the uncoated samples during the polarization process.

Figure 3 clearly evidences that both TiN coatings reduce the current density of the aluminum substrate in the two temperatures (RT and 70 ^{o}C). The current densities of the uncoated Al samples after 1 h at RT and 70 ^{o}C conditions were 78.71 μA cm^{-2} and 78.90 μA cm^{-2} respectively. For the homogeneous TiN film at RT, the current density increases linearly at a rate of 1.71 μA.cm^{-2}.h^{-1} and reaches 3.51 μA.cm^{-2} after 1 h, whereas at 70 ^{o}C it increases at a rate of 5.91 μA.cm^{-2}.h^{-1} up to 11.38 μA.cm^{-2} after 1 h, these values are very close to those reported in the literature for similar materials tested under similar conditions [8]. Finally, for the graded TiN film, after 1 h, the current density reaches 0.56 μA.cm^{-2} at RT and 1. 43 μA.cm^{-2} at 70^{o}C, with increasing rates of 0.25 μA.cm^{-2}.h^{-1} and 0.59 μA.cm^{-2}.h^{-1}, respectively. The increase of the current density in the cathodic environment (70 ^{o}C) was also previously reported in the literature [8, 62].

Clearly, the results of the polarization experiments showed that the current densities values estimated with the different methodologies (potentiodynamic and potentiostatic) for the uncoated aluminum samples

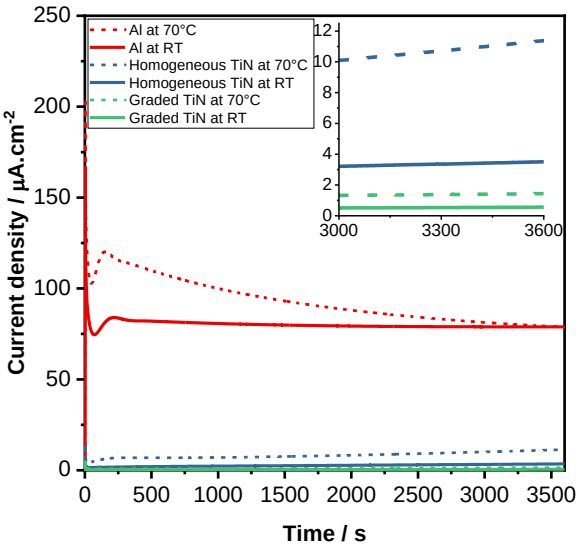

(a)

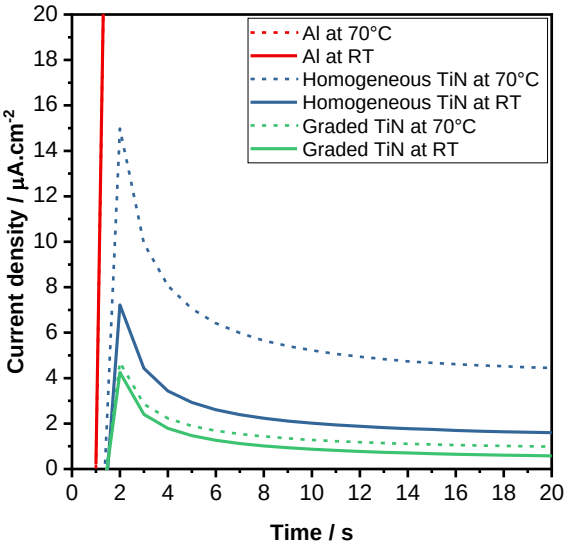

(b)

Figure 3: (a) overall results, enlarged images of the beginning of the process; (b) coated samples.

in both solutions are well above the 1 μA.cm^{-2} threshold recommended by the US DOE as the limiting current density value acceptable for a BPP in operation [19]. On the other hand, for the homogeneous TiN coating current densities values below this threshold were only obtained at the corrosion potential for both electrolyte temperatures tested (Table 1).The graded coating also does not comply with this recommendation when potentiodynamically polarized at +0.6 V (Ag/AgCl): 1.31 μA.cm^{-2} (RT) and 6.98 μA.cm^{-2} (70 ^{o}C) and in the potentiostatic experiment (+0.6 V (Ag/AgCl)) performed at 70^{o}C: 1.43 μA.cm^{-2}. However, in two of these situations the current density remained very close to the threshold established by the US DOE for BPP applications, demonstrating that it is a promising approach to protect aluminum substrates. Finally, it is important to stress that the conditions used in the present investigation seem to be a bit harsher than those employed in the US DOE recommendation. As will be shown in the next paragraphs, the TiN coatings produced by GAMS present a superior behavior than several systems reported in the literature.

Li *et al.* [64] compiled values of i_{corr} and of the potentiostatic current densities of several works [76, 87–94] investigating the corrosion behavior of Al substrates protected with different coatings aiming to their use as BPP, the coatings were deposited by different methodologies. Comparing the information displayed in Table 3 of Li *et al.* [64], and those obtained in the present work, disregarding differences in the specific exposure conditions, the i_{corr} determined at RT in the present work for the graded coating is located well below the values for other configurations. Considering the other tested conditions, only the i_{corr} values of El-Enin *et al.* [92] and Lee *et al.* [93] (0.288 μA.cm^{-2} and 0.33 μA.cm^{-2}, respectively) showed smaller values than those presented in Table 1 of the present work. However, in [92] the concentration of H_2SO_4 was much lower (10^{-4}M), even though the tests were performed at 90 ^{o}C, whereas in [93] the test temperature was 70 ^{o}C in 1M H_2SO_4, according to the information provided by Li *et al.* [64]. Considering the graded sample tested at 70 ^{o}C, the present values of i_{corr} (0.37 μA.cm^{-2}) are similar to those reported by Li *et al.* [64] which exhibited the best performance among the data compiled by these authors. Considering the polarized condition, once again, the graded sample tested at RT outperforms all the systems reported by Li *et al.*[64] and only the behavior found by Mawdsley *et al.* [87] was superior (lower current density) to the remainder of the conditions reported in the present work. However, in this particular reference, the tests were performed at RT in 0.1 M H_2SO_4 and with no addition of fluoride ions, indicating a milder aggressive condition.

Specifically considering TiN coatings, Li *et al.* [64] tested Al BPPs coated with TiN and C/TiN (multilayer but not specified how it was obtained) in 0.001 M H_2SO_4 + 0.1 ppm NaF by means of potentiodynamic and potentiostatic polarization tests. In the potentiodynamic tests the authors report that the TiN coating exhibited a current density value as high as that showed by the uncoated sample at the typical cathode working

potential, whereas their multilayered C/TiN coating showed a current density of 36.0 μA.cm^{-2}, both values clearly much superior when compared with the performance of TiN coatings in the present work (Table 1). Moreover, the analysis of the potentiodynamic polarization curves (Figure 3 [64]) show that their i_{corr} were also superior to those reported in Table 1. Li *et al.* [64] do not mention their i_{corr} values. Considering the potentiostatic tests, the authors [64] tested their samples for about 10 h, however, after 1 h the currents densities of both TiN coatings (single and multilayered) were clearly superior to 200 μA.cm^{-2}, which is largely superior than the values reported in Table 1. As in our work, Li *et al.* [64] also applied a Ti interlayer on the substrate surface, however, their coatings were produced by close field unbalanced magnetron sputter ion plating.

Lee *et al.* [71] also tested the corrosion resistance of a Ti/TiN coating by means of potentiodynamic and potentiostatic polarization tests in an unspecified cathodic environment (the only relevant information was that it was saturated with O_2). The i_{corr} value reported by Lee *et al.* [71] for their Ti/TiN coating in the cathodic environment is clearly larger than those reported in the present work (Table 1). Moreover, the analysis of the anodic polarization curve (Figure 5(b) [71]) shows that it is more depolarized than those presented in Figure 2. For the potentiostatic test (performed at +0.6 V SHE, corresponding to +0.403 Ag/AgCl), the authors [71] report a final current value of 20 μA.cm^{-2} after 8 h. This value is clearly larger than those reported in Table 1, even considering that a more anodic potential was imposed to our system (+0.6 V Ag/AgCl). Lee *et al.* [71] polarized their electrode also for a longer period and also applied a Ti interlayer. Their coating was deposited by electromagnetic-field-superpositioned DC magnetron sputtering.

3.2.2. EIS tests

Figures 4 and 5 present the Nyquist and the Bode plots at RT and at 70 ^{o}C for the uncoated and coated samples acquired after stabilization of the OCP for 1 h. The Nyquist plots, Figure 4, evidence that the diagrams of the uncoated Al substrate are more complex, being composed of a high frequency (HF) capacitive loop, followed by a low frequency (LF) inductive loop and another capacitive loop at even lower frequencies. This kind of response has been reported for aluminum in different media [95, 96]. The origin of the HF capacitive loop is controversial, but it has been frequently associated with the presence of the oxide layer [97], sometimes associated with other processes with similar time constants representing the oxidation of the Al metal [95, 98]. On the other hand, the inductive loop is frequently associated with the relaxation of reaction's intermediate [95, 98–100], and also to relaxation phenomena resulting in active dissolution of aluminium [97, 101]. In this latter case, however, no LF capacitive loop has been reported. Regarding this latter loop, Aoki *et al.* [98] proposed that it could be associated with the relaxation of the passive film

thickness.

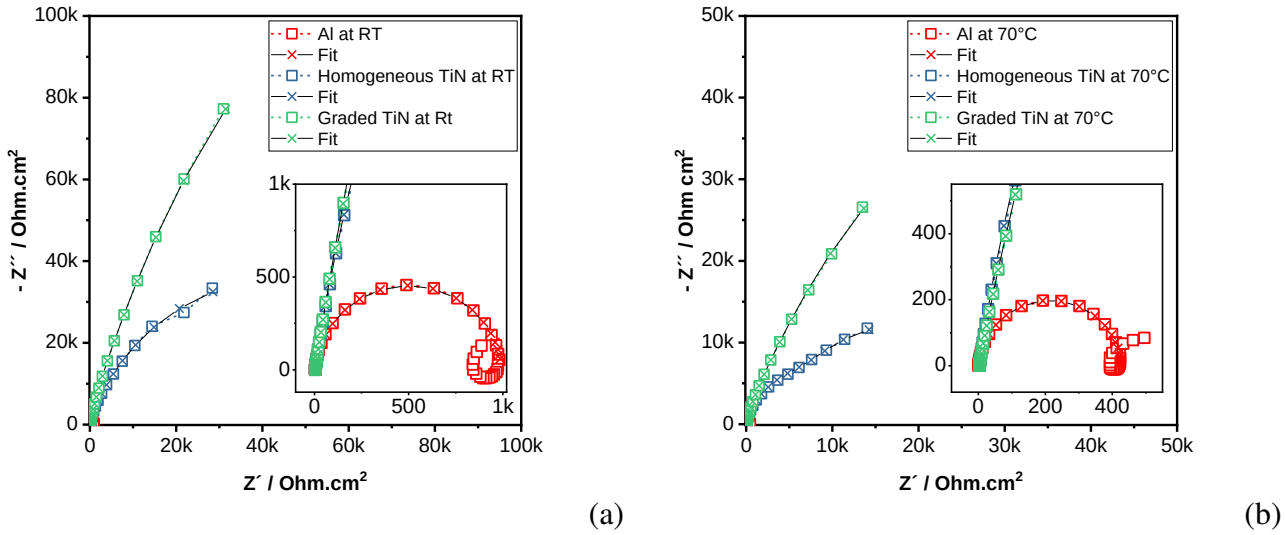

(a) (b)

Figure 4: Nyquist diagrams of the different materials at: (a) RT, (b) 70 °C. Experimental data are presented as open symbols and the fitted data by crosses.

As evidenced by the diagrams in Figures 4 and 5, and in accordance with their better polarization behavior, the coated samples presented higher impedance modulus compared with the uncoated aluminum. For both coated samples, the diagrams are composed of a single wide capacitive loop (Figure 4), whose phase angle is close to 80° (Figure 5). The depressed nature of the phase angle indicates that more than one time constant may overlap in the investigated frequency range, a feature that is particularly evident for the samples protected with the homogeneous TiN coating, for which the phase angle deviates from the capacitive response at LF.

The EIS diagrams also confirm the better corrosion resistance corresponding to the graded TiN coated samples at both temperatures, and demonstrate that, irrespective of the system, the impedance modulus decreases for increasing temperature, confirming the deleterious effect of this variable to corrosion resistance (as expected).

The EIS diagrams shown in Figure 5 corresponding to the coated samples were fitted using the electrical equivalent circuit (EEC) depicted in Figure 6, which is presented associated with the physical model assumed for the interface, in order to better evaluate the quantitative EIS response. In corrosion studies of coated metals, usually using insulating or organic coatings, the HF capacitive time constant is associated to the EIS response of the coating itself (dielectric response in series with the resistance at defective sites) [62, 102]. In the present case, however, the Al substrate is coated with a conductive film (TiN) [103, 104]; therefore, no dielectric response of the TiN coating, which acts as an electron collector, should be expected. Thus, the HF time constant was associated with the double layer charging (Cdl) at the coating surface in

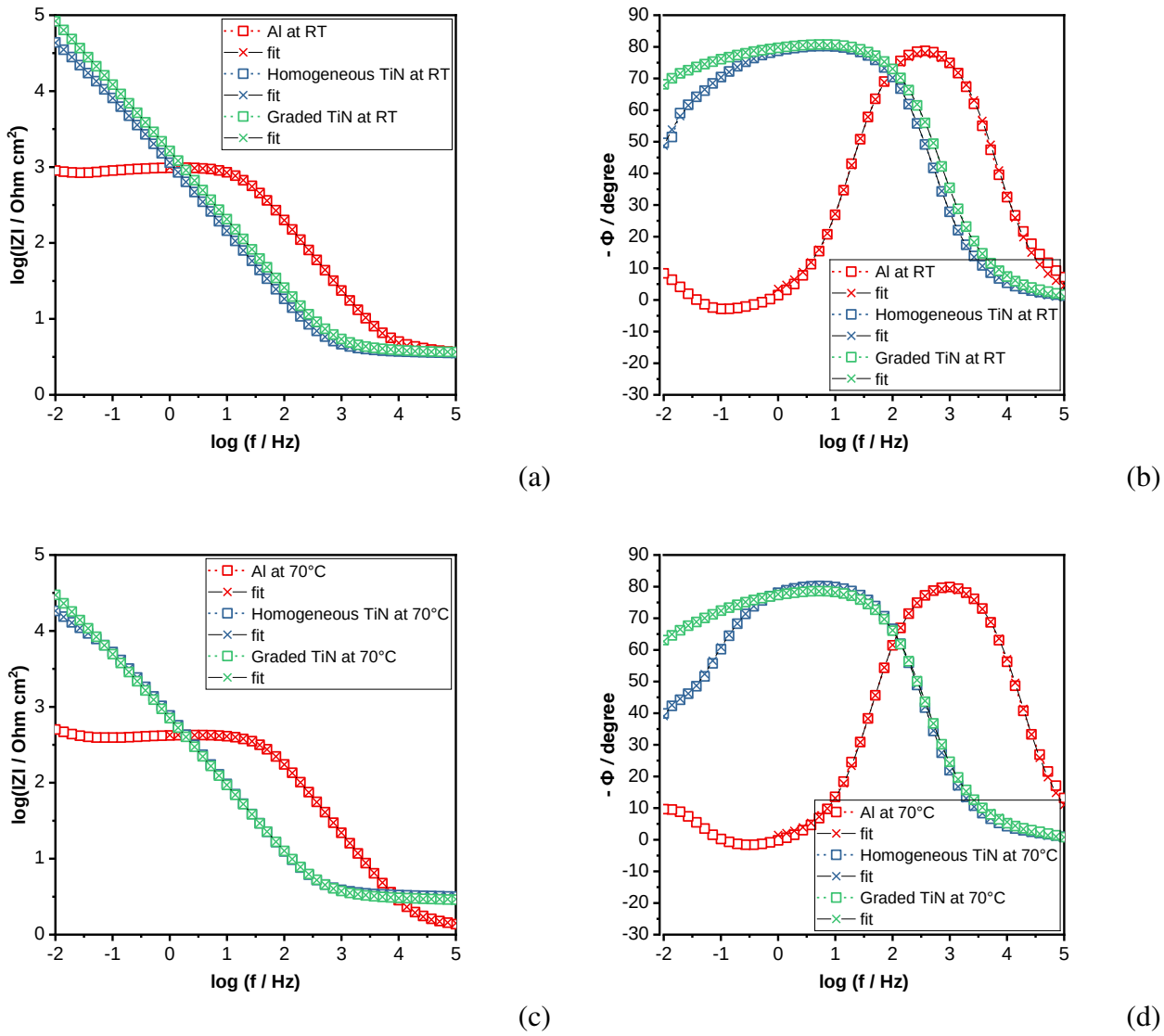

Figure 5: Bode diagrams of the different samples at: (a, b) RT, (c,d) 70°C. Experimental data are presented as open symbols and the fitted data by crosses.

series with a charge transfer resistance reaction (Rct(TiN)), probably associated with the Oxygen Reduction Reaction (ORR). CPE (Ti) corresponds to the response of the Ti interlayer, which is mostly in contact with the TiN coating (thus it receives the current leaking at the coating surface), but it is also wetted by the electrolyte at the bottom of defective sites (pores) of the TiN layer. This interlayer must be protected with an oxide and responds to the potential perturbation with the time constant CPE(Ti)/Rpo(Ti), whose resistive component corresponds to the resistive response developed on the pores of the oxide layer (no electrochemical response of the bare Ti could be detected in the investigated frequency range and short immersion time, as it remains in the passive state). Finally, a diffusion-controlled process, represented by a Warburg (W) impedance, was identified, probably taking place within the pores of the TiN layer, and Rs accounts for the uncompensated electrolyte resistance.

In the EEC of Figure 6, a pure capacitor was used to represent the double layer capacity at the coating

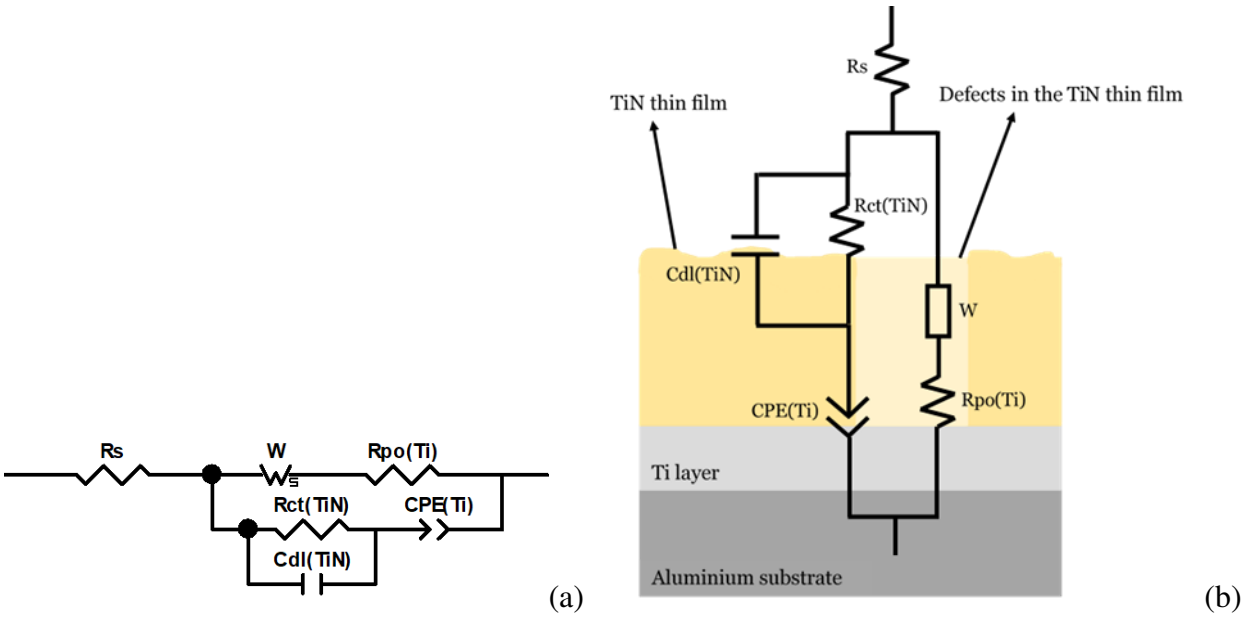

Figure 6: a) Electrical equivalent circuits used to fit the EIS results of the TiN coated samples b) physical model of the interface.

surface (Cdl(TiN)), whereas a constant phase element (CPE) was employed to fit the capacitive response of the Ti oxide layer (CPE(Ti)), which is in contact both with the TiN coating and with the electrolyte at the TiN pores bottom. In EEC fitting procedures, pure capacitors are replaced by CPE to account for non-ideal behavior of the capacitance [105, 106]. The impedance of a CPE is given by Equation (1), where T is a constant in F.cm^{-2}.s^{n-1}, n is associated to the rotation angle of a purely capacitive response in the Nyquist plot [107, 108], and j and ω have their usual meaning. Note that in cases in which n = 1 the CPE behaves as a pure capacitor:

$$Zcpe = \frac{1}{T(j\omega)^n} \tag{1}$$

In Figures 4 and 5 the results of the fitting procedures for the coated samples are presented by crosses, whereas the experimental results are represented by open symbols. The goodness of the fitting can be ascertained by the good match between the experimental and fitted data, as well as by the low chi-squared values, all below 2 x 10^{-4}. The authors emphasise that fittings with simpler EECs were tried; however, the quality of the fitting was inferior and, in addition, some of the fitted parameters presented values that were not physically acceptable [109]. Finally, the fitting for the uncoated samples was performed using a simple Randles circuit, with a CPE replacing the pure capacitance, and considering only the high frequency capacitive loop of the diagrams. This procedure was adopted only to compare the order of magnitude of the resistive elements.

Table 2 displays the results of the fitting procedure. The responses of the electrochemical processes at

the coatings surfaces show that the capacity values (Cdl(TiN)) are in good agreement with those frequently associated with the double layer capacity, between 10 and 50 μF.cm^{-2} [110, 111]. The higher values may be attributed to surface roughness, increasing the effective exposed area, on the other hand Rct(TiN) was very low. This latter feature indicates that the coating surface is an excellent electronic collector and opposes very low resistance to electron (current) flow, which is an interesting property for BPP application. The low Rct value explains why a clear HF time constant is not verified in the Bode plots.

Table 2: Results of the fitting procedure of the EIS diagrams with the EEC of Figure 6 for the samples coated with homogeneous and graded TiN at both test temperatures. The results for the uncoated samples correspond to the fitting of the HF capacitive loop with a Randles circuit.

Condition	Al RT	Al 70°C	Homogeneous TiN RT	Homogeneous TiN 70°C	Graded TiN RT	Graded TiN 70°C
Rs (Ω.cm^2)	3.82	1.36	3.57	3.20	3.67	2.92
Rct(Al) (Ω.cm^2)	935	421	-	-	-	-
CPE(Al) (F cm^{-2}.s$^{(n-1)}$)	1.06x10^{-5}	1.09x10^{-5}	-	-	-	-
n(CPE(Al))	0.95	0.95	-	-	-	-
Rct(TiN) (Ω.cm^2)	-	-	0.23	0.21	0.31	0.25
Cdl(TiN) (F cm^{-2})	-	-	8.60x10^{-5}	9.72x10^{-5}	7.12x10^{-5}	1.10x10^{-4}
W (Ω.cm^2)	-	-	7.99x10^4	1.83x10^4	3.97x10^5	1.16x10^5
n(W)	-	-	0.40	0.54	0.45	0.45
Rpo(Ti) (Ω.cm^2)	-	-	1.04x10^4	1.11x10^4	1.52x10^4	5.63x10^3
CPE (Ti) (F cm^{-2}. s$^{(n-1)}$)	-	-	1.59x10^{-4}	2.37x10^{-4}	1.13x10^{-4}	2.64x10^{-4}
n(CPE(Ti))	-	-	0.91	0.91	0.91	0.90
Rs+W+Rct(Ti)	-	-	9.03x10^4	2.94x10^4	4.12x10^5	1.22x10^5

The other circuit elements are related to the electrochemical processes basically occurring at the pores bottom (defective sites of the TiN layer) and at the interface between the Ti-interlayer and the TiN coating. The trend for the T value of the CPE(Ti) component showed higher values for the samples tested at 70 °C, indicating increased water penetration (higher dielectric constant due to water uptake) and/or larger exposed area. However, the accurate analysis of this variable is impaired due to the fact that it is representative of the processes taking place underneath both the intact TiN coating and at its flaws. The exponents of the CPEs were all close to 0.9, indicating a fairly capacitive behavior for the oxide layer formed on the Ti interlayer. Finally, the exponents of the diffusion processes were between 0.4 and 0.54 indicating an almost perfect diffusion control (ideal value = 0.5).

The values of the resistive elements can be more straightforwardly associated with the corrosion resistance. It is clear that, whatever the coating system and test temperature, the resistance associated with the diffusion process (W) within the narrow pores of the TiN coating is the dominant effect. Considering the effect of temperature, the impedance of the samples protected with the graded TiN coating is about 4.5 and 4 times higher than the homogeneous film at RT and 70 °C, respectively. In general, according to the resistance values, the corrosion resistance can be classified as graded TiN RT > graded TiN 70 °C > homogeneous TiN RT > homogeneous TiN 70 °C, which is in fully agreement with the i_{corr} tendency determined

in the anodic polarization experiments and reported in Table 1. Finally, both at RT and 70 ^{o}C the impedance of the samples protected with the graded TiN films are close to 3 orders of magnitude higher than that of the uncoated aluminium, whereas this increase was about two orders of magnitude for the samples protected with the homogeneous TiN coating.

3.3. Correlation with the film microstructure

As the electrochemical tests show, the graded TiN coating has a superior behavior regarding corrosion in all media investigated. A question can be posed to understand what characteristic features of the film would be responsible for this improved result.

In a previous work by some of the present authors [67], the microstructures of the homogeneous and graded TiN thin films were investigated using scanning electron microscopy (SEM). The observation of the films cross-sections showed that the produced layers were about 1.0-1.5 μm thick and with no cracks at the interface with the substrate. In addition, in Figure 7 detailed TEM analysis showed that the films were compact, and no voids or pores could be observed even in the nanometer scale. The SEM analysis of fractured samples also revealed that both films presented a columnar structure with grains sizes of about 50 nm, even though at the samples surface the homogeneous coating showed equiaxed features [67].

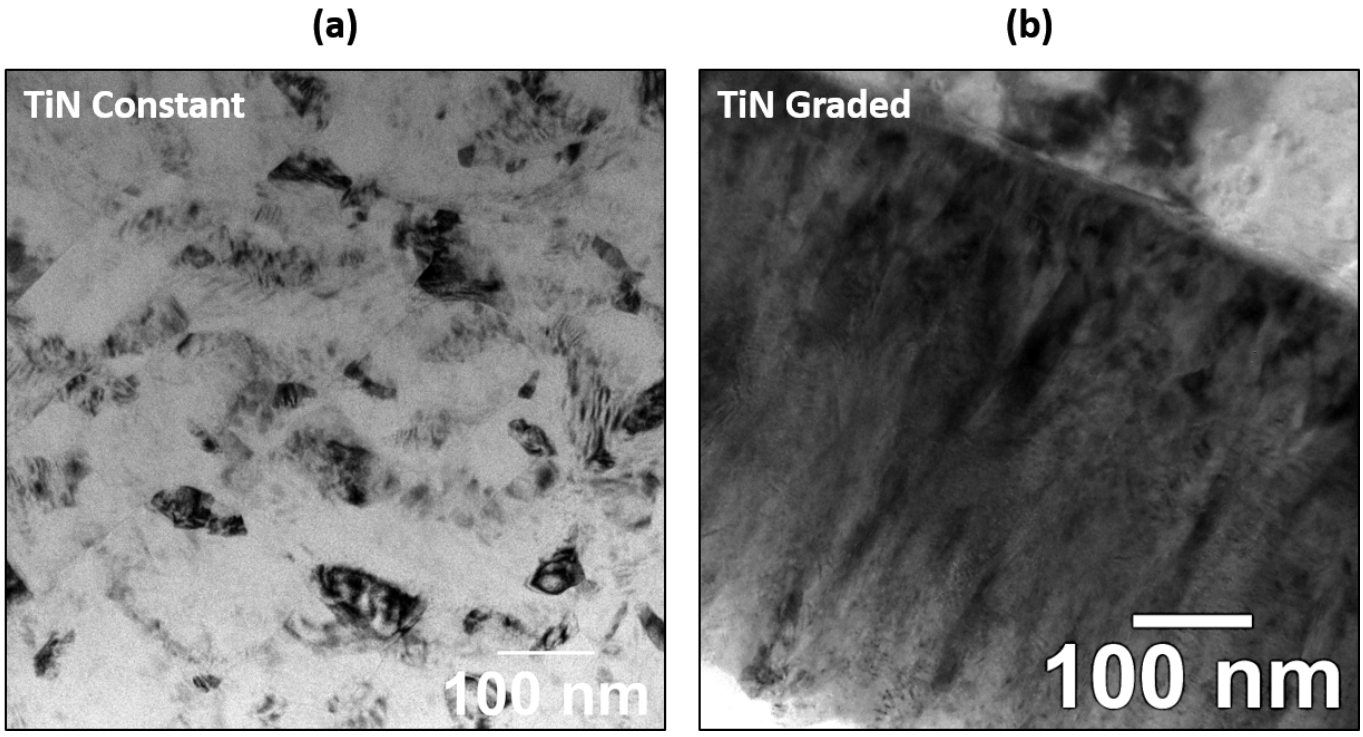

Figure 7: TEM investigations on the microstructure of both TiN (a) homogeneous and (b) graded thin films. Detailed analysis on the microstructure of both TiN thin films can be found elsewhere [67]. Note: both micrographs were recorded using BFTEM mode.

Grazing incidence x-ray diffraction (GIXRD) patterns for homogeneous and graded TiN films (the same

used in this present work) [67] are showed in Figure 8 and indicated strong (200) and (111) crystallographic orientation, respectively. The (111) crystallographic orientation has been frequently reported for TiN coatings prepared by different methodologies and applied to different substrates [58, 112, 113], whereas, planes of the zone {100} were also reported in some cases [114, 115]. Several works show that a change in N_2 flow rate affects the crystallografic orientation [114, 115]. However, the change in the crystallografic orientation also depends on the other deposition parameters as extensively discussed by Mahieu and Depla [66]. According them, one determinant parameter for crystallografic orientation of sputtered TiN films is the atomic N/Ti flux ratio. A transition from (111) to (200) tends to occur when the N/Ti flux ratio increases [66]. For depositions in similar conditions, the increase in N_2 flow rate should raise the N/Ti flux ratio. It can explain the (111) preferred orientation of the graded film and the (200) preferred orientation of the homogeneous film, once that the N_2 flow rate is kept low in the beginning of graded film deposition.

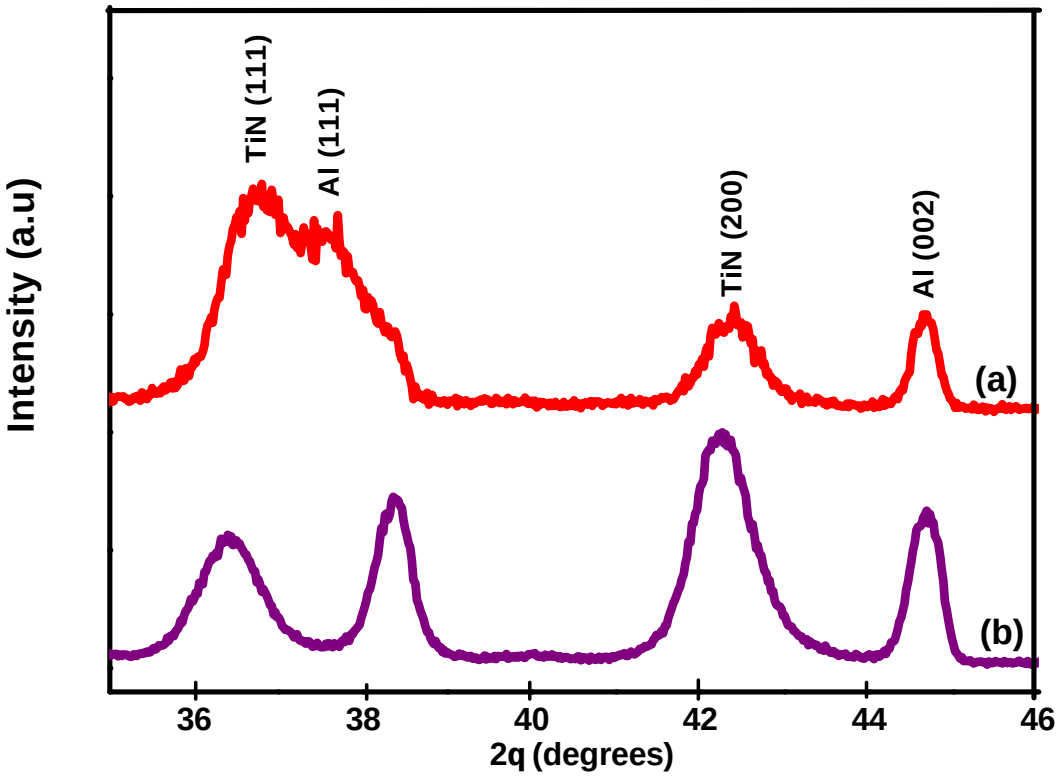

Figure 8: GIXRD TiN patterns (a) graded and (b) homogeneous film.Adapted from [67, 68].

It is well-known that good adhesion between coatings and substrates is an important prerequisite for increased corrosion resistance as this hinders delamination and, consequently, the penetration and accumulation of aggressive species at the coating/substrate interface [116–118]. Some authors applied Ti interlayer

with a thickness range 75 nm - 1 μm to increase corrosion resistance [119–122] and improve adhesion of TiN-PVD coatings [122–124]. This layer is effective, and creates a barrier against harshly corrosive media. This hinders the formation of defects that can serve as open paths to ions species reaching the substrate. In this study, all films (both homogeneous and graded) had Ti interlayers of about 150 nm. Therefore, with the exception of the preferred orientations of the films, almost all characteristics are the same in both films [68].

Some authors have suggested relationships between adhesion, microstructure and crystal orientation [58, 125]. Shan *et al.* [125] reported that columnar structures and strong (111) preferred orientation for homogeneous TiN films deposited by PVD may increase the adhesion properties. Conversely, Cui *et al.* [58] reported increased adhesive bond of graded TiN films when compared to homogeneous film, which was attributed to the absence of sharp changes in chemistry and crystal structure due to the gradual increase of nitrogen content within the coating. However, in Cui *et al.* [58] work, homogeneous TiN coatings showed columnar structure and (111) crystallography orientation, whereas the graded coating presented a featureless compact microstructure, which was different from the tendency observed in the present investigation. Since Cui *et al.* [58] obtained their coating by dc magnetron sputtering deposition, the differences can be attributed to the different deposition conditions, which affects the microstructure [126–129], as well crystallographic orientation [66].

Kumar *et al.* [115] deposited nanocrystalline TiN/NiTi thin films by dc magnetron sputtering and examined the effect of crystallographic orientation of TiN. The nanocrystalline TiN with crystallographic orientation (200) showed increased corrosion resistance, effect which was ascribed to a higher real surface area (with smaller grains) and a more homogeneous surface. However, in the present investigation the results of the microstructural characterization showed similar grain sizes for both samples, therefore, the reasoning of Kumar *et al.* [115] cannot be applied to the present investigation.

In the case of ZrN films deposited onto metallic substrates using magnetron sputtering technique Larijani *et al.* [130] verified increased corrosion resistance with (111) crystallographic orientation. The authors attributed this behavior to the close packed structure and chemical stability of the (111) crystallographic orientation. Hence, since in the present investigation the grain sizes for both homogeneous and graded films were similar, it can be suggested that the (111) crystallographic orientation of the graded film may contribute to the increased corrosion resistance.

Certainly a change in crystal orientation for the film results in flaws of different natures, this is a possible origin of the improved corrosion resistance of the graded TiN film, when compared with the homogeneous film. However, there is a possible intrinsic reason associated with the graded film which could justify such

improved performance: the nitrogen gradient observed along thickness [67]. This will be discussed next.

3.4. Functionally graded TiN film plasmonics and corrosion resistance

In electron energy loss spectroscopy, the observed spectrum is a result of interaction between the electron beam with the electrons of the valence band of the sample [131]. One of the aspects of this interaction is the generation of plasmons in the sample. The analysis of these plasmons from the EELS spectra, therefore, will allow to probe the properties of these valence electrons.

The most significant result obtained with EELS analysis is shown in Figure 9(a-b). This analytical characterization shows that first plasmon energy loss peak presents a negative shift for lower energy losses from the border of the graded TiN film towards the Al substrate. These results can be explained by means of the relationship between the plasmon energy loss (E_{lp}) and its oscillation frequency (ω_p), given by [132–135]:

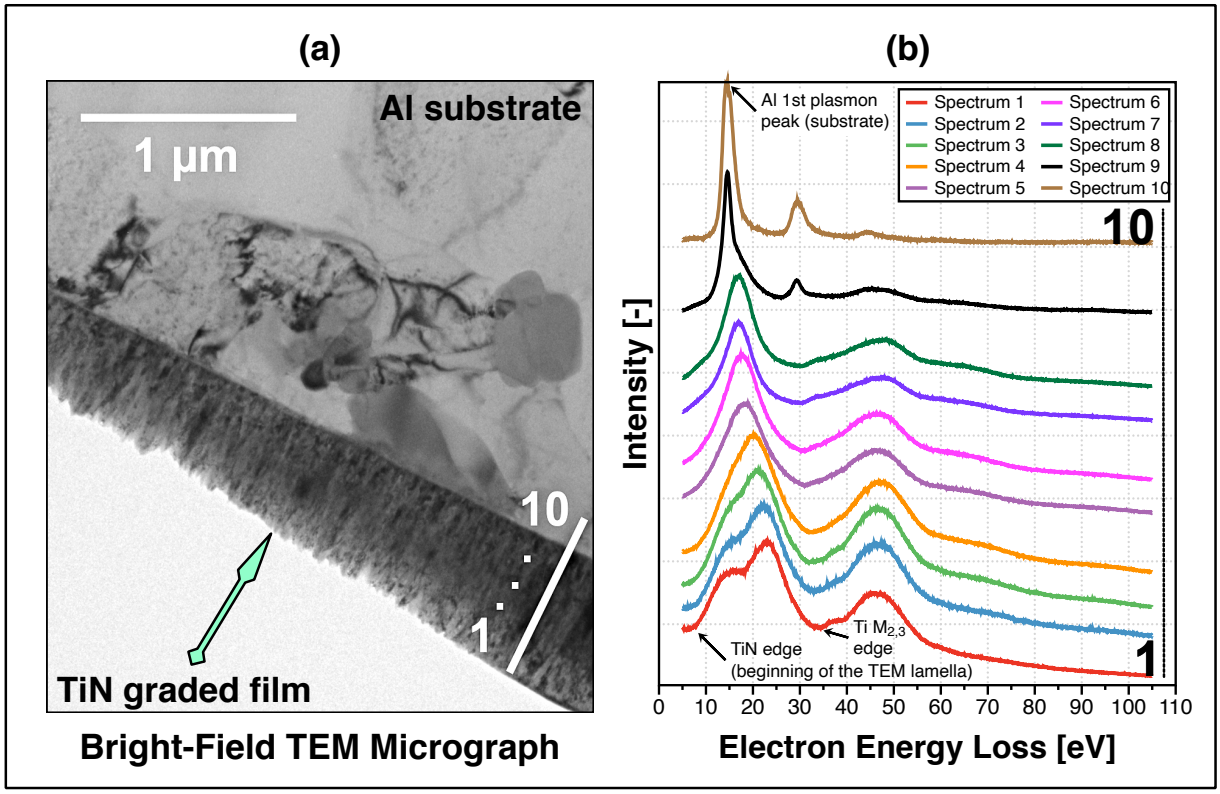

Figure 9: Plasmonic analysis of the graded TiN film: (a) Low-magnification BFTEM micrograph showing the film-substrate system where the white-line represents the EELS analyzed areas (from the beginning of the film to the Al substrate) associated with the low-loss spectra in figure (b). Note: in the figure (b) both the Al first plasmon peak at 15 eV and Ti $M_{2,3}$ major edge at 35 eV were indexed using the available in literature [136].

$$E_{lp} = \hbar\omega_p = \hbar\sqrt{\frac{ne^2}{\epsilon_0 m_e}} \tag{2}$$

where n is the density of valence electrons, e and m_e the electron charge and mass, respectively, and the

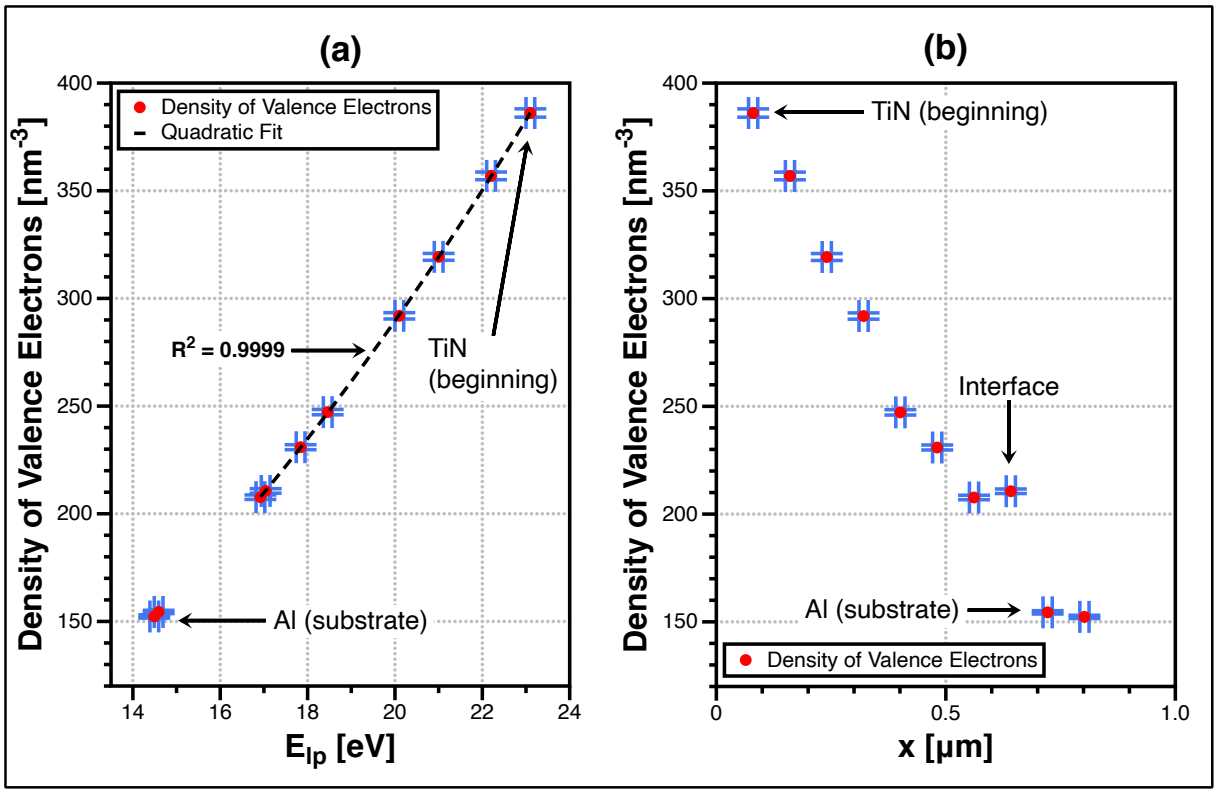

Figure 10: Quantitative data extracted from the low-loss EELS measurements: the estimated density of valence electrons as function of (a) the plasmon energy and (b) the film thickness profile.

$\epsilon_0 = 8.8542 \times 10^{-12}$ F m^{-1} is the vacuum permittivity. Equation 2 was derived considering the oscillation of free electrons in vacuum, although it can be applied in good approximation for certain materials, including Al and Ti, as previously studied by Colliex [131, 137]. It can be noticed that the density of valence electrons is directly proportional to the plasmon energy loss. From the edge of the graded TiN film up to the interface with the Al substrate, E_{lp} has been observed to be significantly reduced. This decrease shows the variation of N concentration along thickness, as anticipated for the graded film, and consistent with independent XPS measurements [67]. After the interface, EELS spectra reveals that the Al substrate posses a rather different electronic configuration, as expected. Similar analysis was recently made to estimate the content of hydrogen in Zr hydrides [135], for example.

With the low-loss EELS analysis presented in Figure 9 and with the relationship expressed by equation 2, it was possible to estimate the density of valence electrons as function of both plasmon energy and the graded TiN film thickness profile. These results are shown, respectively, Figure 10(a) and (b).

The electrochemical processes responsible for the corrosion of the TiN layer naturally depend on the electron concentration in the valence band, since these are the electrons which interact with the ions in the electrolyte. The electron concentration of the film surface must be similar for both films since deposition ends in the same way in both cases. However, as the corrosion process is established, the electrolyte

begins to interact with deeper layers of the film. In the case of the graded sample, these deeper layers are characterised by a lower valence electron concentration, and this must result in a lower corrosion rate.

4. Conclusions

Our study demonstrates that aluminum substrates can be successfully protected against corrosion in a corrosive media expected for PEMFCs by using TiN/Ti thin films deposited by GAMS. The results of the electrochemical investigation of coated samples tested both at room temperature and at 70 ^{o}C in a cathodic-like environment (H_2SO_4 saturated with O_2) showed an effective reduction of the corrosion current densities both at the corrosion potential and under polarization conditions similar to those encountered in PEMFC as well as an increase in the impedance modulus at the OCP.

The application of a graded coating, with increasing N content from the bottom (metallic substrate) to the surface, showed improved corrosion resistance when compared with the homogeneous coating. Al samples protected with this particular coating showed corrosion current density well below the threshold established by the DOE as acceptable for fuel cell application (1.0 μA.cm^{-2}), whereas the anodic current density remained close to this value when the tests were performed under polarization conditions close to those used at the cathode compartment of a PEMFC. Moreover, the TiN graded coating outperforms other similar coatings deposited using different methodologies, indicating that GAMS is a promising methodology for obtaining corrosion resistant coatings.

The improved corrosion resistance of the graded thin film can be attributed both to an extrinsic factor as the change of orientation due to the film growth mode, and to intrinsic factors as the reduced valence electron concentration observed close to the substrate in the graded films, and increased adherence of the graded substrate to the Ti seed layer applied on top of the Al substrate, hindering the corrosion process, as indicated by the EIS fitting procedure.

Acknowledgments

This project was partially funded by the Foundation of Support for Research and Innovation of the Santa Catarina State (FAPESC) under contract PAP-TR 781. The authors would like to thanks Prof. A.B. Henriques at the Institute of Physics of the University of São Paulo and Dr. A. Mir at the University of Huddersfield by the useful discussions on plasmons. CGS wishes to acknowledge the financial support by the Brazilian National Research, Technology and Innovation Council (CNPq) under grant 308565/2018-5. MAT was supported through the ASTRO fellowship, a United States Department of Energy workforce development program implemented at Oak Ridge National Laboratory through the Oak Ridge Institute for

Science and Education under contract DE-AC05-06OR23100. MAT would like to thank Professor Stefan Pogatscher (MU Leoben) to currently support his post-doctoral research under the European Research Council (ERC) excellent science grant "TRANSDESIGN" through the Horizon 2020 programme under contract number 757961.

References

[1] N. Simcock, Energy, in: A. Kobayashi (Ed.), International Encyclopedia of Human Geography (Second Edition), second edition Edition, Elsevier, Oxford, 2020, pp. 123 – 135. doi:https://doi.org/10.1016/B978-0-08-102295-5.10783-8.

[2] R. Albertyn, H. Rode, A. J. W. Millar, M. Peck, The domestication of fire: The relationship between biomass fuel, fossil fuel and burns, Burns 38 (6) (2012) 790–795.

[3] M. Suzuki, N. Kanie, M. Iguchi, New approaches for transitions to low fossil carbon societies: promoting opportunities for effective development, diffusion and implementation of technologies, policies and strategies, Journal of Cleaner Production 128 (2016) 1–5.

[4] L. Stemper, M. A. Tunes, P. Oberhauser, P. J. Uggowitzer, S. Pogatscher, Age-hardening response of almgzn alloys with cu and ag additions, Acta Materialia 195 (2020) 541 – 554. doi:https://doi.org/10.1016/j.actamat.2020.05.066.

[5] L. Stemper, B. Mitas, T. Kremmer, S. Otterbach, P. J. Uggowitzer, S. Pogatscher, Age-hardening of high pressure die casting almg alloys with zn and combined zn and cu additions, Materials & Design 181 (2019) 107927.

[6] D. Medvedev, Trends in research and development of protonic ceramic electrolysis cells, International Journal of Hydrogen Energy 44 (49) (2019) 26711–26740.

[7] R. O'hayre, S.-W. Cha, W. Colella, F. B. Prinz, Fuel cell fundamentals, John Wiley & Sons, 2016.

[8] E.-K. Lee, J.-K. Kim, T.-J. Kim, H. Song, J.-H. Kim, S.-A. Park, T.-G. Jeong, S.-W. Yun, J. Lee, J. Goo, others, Enhanced corrosion resistance and fuel cell performance of Al1050 bipolar plate coated with TiN/Ti double layer, Energy conversion and management 75 (2013) 727–733.

[9] V. Vishnyakov, Proton exchange membrane fuel cells, Vacuum 80 (10) (2006) 1053–1065.

[10] J. Shi, P. Zhang, Y. Han, H. Wang, X. Wang, Y. Yu, J. Sun, Investigation on electrochemical behavior and surface conductivity of titanium carbide modified ti bipolar plate of pemfc, International Journal of Hydrogen Energy 45 (16) (2020) 10050–10058.

[11] P. Yi, D. Zhang, D. Qiu, f. Peng, X. Lai, Carbon-based coatings for metallic bipolar plates used in proton exchange membrane fuel cells, Int. J. Hydrogen Energy 44 (13) (2019) 6813–6843. doi:10.1016/j.ijhydene.2019.01.176.

[12] S. Y. Tsai, C. Y. Bai, C. H. , G. N. Shi, K. H. Hou, Y. M. Liu, M. D. Ger, The characteristics and performance of electroless nickel and immersion Au plated aluminum alloy bipolar plates in polymer electrolyte membrane fuel cells, J. Power Sources 214 (2012) 51–58. doi:10.1016/j.jpowsour.2012.04.030.

[13] P. Yi, L. Zhu, C. Dong, K. Xiao, Corrosion and interfacial contact resistance of 316L stainless steel coated with magnetron sputtered ZrN and TiN in the simulated cathodic environment of a proton-exchange membrane fuel cell, Surf. Coatings Technol. 363 (October 2018) (2019) 198–202. doi:10.1016/j.surfcoat.2019.02.027.

[14] F. Bi, P. Yi, T. Zhou, f. Peng, X. Lai, Effects of Al incorporation on the interfacial conductivity and corrosion resistance of

CrN film on SS316L as bipolar plates for proton exchange membrane fuel cells, International Journal of Hydrogen Energy 40 (31) (2015) 9790–9802.

[15] F. Madadi, A. Rezaeian, H. Edris, M. Zhiani, Improving performance in PEMFC by applying different coatings to metallic bipolar plates, Materials Chemistry and Physics 238 (2019) 121911.

[16] T. Wilberforce, O. Ijaodola, E. Ogungbemi, F. Khatib, T. Leslie, Z. El-Hassan, J. Thomposon, A. Olabi, Technical evaluation of proton exchange membrane (PEM) fuel cell performance–A review of the effects of bipolar plates coating, Renewable and Sustainable Energy Reviews 113 (2019) 109286.

[17] P. Yi, D. Zhang, D. Qiu, f. Peng, X. Lai, Carbon-based coatings for metallic bipolar plates used in proton exchange membrane fuel cells, International Journal of Hydrogen Energy (2019).

[18] Y. Awin, N. Dukhan, Experimental performance assessment of metal-foam flow fields for proton exchange membrane fuel cells, Appl. Energy 252 (June) (2019) 113458. doi:10.1016/j.apenergy.2019.113458.

[19] R. A. Antunes, M. C. L. Oliveira, G. Ett, V. Ett, Corrosion of metal bipolar plates for PEM fuel cells: A review, International journal of hydrogen energy 35 (8) (2010) 3632–3647.

[20] A. Manso, F. Marzo, X. Garicano, C. Alegre, A. Lozano, F. Barreras, Corrosion behavior of tantalum coatings on aisi 316l stainless steel substrate for bipolar plates of pem fuel cells, International Journal of Hydrogen Energy (2020).

[21] J. D. Arregui-Mena, R. N. Worth, G. Hall, P. D. Edmondson, A. B. Giorla, T. D. Burchell, A review of finite element method models for nuclear graphite applications, Archives of Computational Methods in Engineering 27 (1) (2020) 331–350.

[22] P. Mukhopadhyay, R. K. Gupta, Graphite, Graphene, and their polymer nanocomposites, CRC press, 2012.

[23] S. Simaafrookhteh, M. Khorshidian, M. Momenifar, Fabrication of multi-filler thermoset-based composite bipolar plates for pemfcs applications: Molding defects and properties characterizations, International Journal of Hydrogen Energy (2020).

[24] P. Chen, F. Fang, Z. Zhang, W. Zhang, Y. Wang, Self-assembled graphene film to enable highly conductive and corrosion resistant aluminum bipolar plates in fuel cells, International Journal of Hydrogen Energy 42 (17) (2017) 12593–12600.

[25] f. Peng, P. Yi, X. Lai, Design and manufacturing of stainless steel bipolar plates for proton exchange membrane fuel cells, international journal of hydrogen energy 39 (36) (2014) 21127–21153.

[26] L. Wang, Y. Tao, Z. Zhang, Y. Wang, Q. Feng, H. Wang, H. Li, Molybdenum carbide coated 316L stainless steel for bipolar plates of proton exchange membrane fuel cells, International Journal of Hydrogen Energy 44 (10) (2019) 4940–4950.

[27] Y. Hung, H. Tawfik, D. Mahajan, Durability and characterization studies of chromium carbide coated aluminum fuel cell stack, International Journal of Hydrogen Energy 41 (28) (2016) 12273–12284.

[28] H. Wang, J. Turner, Reviewing metallic PEMFC bipolar plates, Fuel Cells 10 (4) (2010) 510–519.

[29] S. Joseph, J. McClure, P. Sebastian, J. Moreira, E. Valenzuela, Polyanie and polypyrrole coatings on aluminum for PEM fuel cell bipolar plates, Journal of Power Sources 177 (1) (2008) 161–166.

[30] A. Bolouri, C. G. Kang, Study on dimensional and corrosion properties of thixoformed A356 and AA7075 aluminum bipolar plates for proton exchange membrane fuel cells, Renewable energy 71 (2014) 616–628.

[31] L. Wang, Y. Tao, Z. Zhang, Y. Wang, Q. Feng, H. Wang, H. Li, Molybdenum carbide coated 316L stainless steel for bipolar plates of proton exchange membrane fuel cells, International Journal of Hydrogen Energy 44 (10) (2019) 4940–4950.

[32] C. Alegre, L. Álvarez Manuel, R. Mustata, L. Valiño, A. Lozano, F. Barreras, Assessment of the durability of low-cost

Al bipolar plates for High Temperature PEM fuel cells, International Journal of Hydrogen Energy 44 (25) (2019) 12748–12759.

[33] A. Bolouri, C. G. Kang, Study on dimensional and corrosion properties of thixoformed A356 and AA7075 aluminum bipolar plates for proton exchange membrane fuel cells, Renew. Energy 71 (2014) 616–628. doi:10.1016/j.renene.2014.06.021.

[34] D. Zhang, L. Duan, L. Guo, Z. Wang, J. Zhao, W.-H. Tuan, K. Niihara, TiN-coated titanium as the bipolar plate for PEMFC by multi-arc ion plating, International journal of hydrogen energy 36 (15) (2011) 9155–9161.

[35] Y. Hung, K. El-Khatib, H. Tawfik, Testing and evaluation of aluminum coated bipolar plates of PEM fuel cells operating at 70 C, Journal of Power Sources 163 (1) (2006) 509–513.

[36] X. Cheng, Z. Shi, N. Glass, L. Zhang, J. Zhang, D. Song, Z.-S. Liu, H. Wang, J. Shen, A review of PEM hydrogen fuel cell contamination: Impacts, mechanisms, and mitigation, Journal of Power Sources 165 (2) (2007) 739–756.

[37] A. LaConti, M. Hamdan, R. McDonald, Mechanisms of membrane degradation, Handbook of fuel cells (2010).

[38] S. Joseph, J. C. McClure, R. Chianelli, P. Pich, P. Sebastian, Conducting polymer-coated stainless steel bipolar plates for proton exchange membrane fuel cells (PEMFC), International Journal of Hydrogen Energy 30 (12) (2005) 1339–1344.

[39] Y. Wang, D. O. Northwood, An investigation into polypyrrole-coated 316L stainless steel as a bipolar plate material for PEM fuel cells, Journal of Power Sources 163 (1) (2006) 500–508.

[40] Y. Wang, D. O. Northwood, An investigation into the effects of a nano-thick gold interlayer on polypyrrole coatings on 316L stainless steel for the bipolar plates of PEM fuel cells, Journal of power sources 175 (1) (2008) 40–48.

[41] M. F. Khan, A. Y. Adesina, Z. M. Gasem, Electrochemical and electrical resistance behavior of cathodic arc PVD TiN, CrN, AlCrN, and AlTiN coatings in simulated proton exchange membrane fuel cell environment, Materials and Corrosion 70 (2) (2019) 281–292.

[42] H. Haghighat Ghahfarokhi, A. Saatchi, S. Monirvaghefi, Corrosion investigation of chromium nitride and chromium carbide coatings for PEM fuel cell bipolar plates in simulated cathode condition, Fuel Cells 16 (3) (2016) 356–364.

[43] E. Haye, F. Deschamps, G. Caldarella, M.-L. Piedboeuf, A. Lafort, H. Cornil, J.-F. Colomer, J.-J. Pireaux, N. Job, Formable chromium nitride coatings for proton exchange membrane fuel cell stainless steel bipolar plates, International Journal of Hydrogen Energy (2020).

[44] J. Jin, M. Hu, X. Zhao, Investigation of incorporating oxygen into tin coating to resist high potential effects on pemfc bipolar plates in vehicle applications, International Journal of Hydrogen Energy (2020).

[45] K. Feng, Z. Li, X. Cai, P. K. Chu, Silver implanted 316L stainless steel as bipolar plates in polymer electrolyte membrane fuel cells, Materials Chemistry and Physics 126 (1-2) (2011) 6–11.

[46] R. Taherian, A review of composite and metallic bipolar plates in proton exchange membrane fuel cell: Materials, fabrication, and material selection, Journal of Power Sources 265 (2014) 370–390.

[47] Y. Leng, P. Ming, D. Yang, C. Zhang, Stainless steel bipolar plates for proton exchange membrane fuel cells: Materials, flow channel design and forming processes, Journal of Power Sources 451 (2020) 227783.

[48] Y. Xie, Y. Wang, H. Du, Electrochemical capacitance performance of titanium nitride nanoarray, Materials Science and Engineering: B 178 (20) (2013) 1443–1451.

[49] B. Yuan, M. Yang, H. Zhu, Titanium nitride nanopowders produced via sodium reductionin liquid ammonia, Journal of Materials Research 24 (2) (2009) 448–451.

[50] T. Zhou, D. Liu, Y. Zhang, T. Ouyang, J. Suo, Microstructure and hydrogen impermeability of titanium nitride thin films deposited by direct current reactive magnetron sputtering, Journal of Alloys and Compounds 688 (2016) 44–50.

[51] M. Zhang, X. Liu, H. Shang, J. , Comparison of TiN and CNx coatings on orthodontic stainless steel: Tribological and biological evaluation, Surface and Coatings Technology 362 (2019) 381–387.

[52] B. Beake, L. Ning, C. Gey, S. Veldhuis, A. Komarov, A. Weaver, M. Khanna, G. Fox-Rabinovich, Wear performance of different PVD coatings during hard wet end milg of H13 tool steel, Surface and Coatings Technology 279 (2015) 118–125.

[53] S. Lee, Mechanical properties of TiNx/Cr1- xN thin films on plasma nitriding-assisted AISI H13 steel, Surface and Coatings Technology 193 (1-3) (2005) 55–59.

[54] K. Bobzin, T. Brögelmann, N. Kruppe, M. Carlet, Wear behavior and thermal stability of HPPMS (al, ti, cr, si) ON,(Al, ti, cr, si) n and (ti, al, cr, si) n coatings for cutting tools, Surface and Coatings Technology (2020) 125370.

[55] S. Ghasemi, A. Shanaghi, P. K. Chu, Nano mechanical and wear properties of multi-layer Ti/TiN coatings deposited on Al 7075 by high-vacuum magnetron sputtering, Thin Solid Films 638 (2017) 96–104.

[56] E. Zalnezhad, A. A. Sarhan, M. Hamdi, Investigating the fretting fatigue life of thin film titanium nitride coated aerospace Al7075-T6 alloy, Materials Science and Engineering: A 559 (2013) 436–446.

[57] V. Merie, M. Pustan, G. Negrea, C. Brleanu, Research on titanium nitride thin films deposited by reactive magnetron sputtering for MEMS applications, Applied Surface Science 358 (2015) 525–532.

[58] W. Cui, G. Qin, J. Duan, H. Wang, A graded nano-TiN coating on biomedical Ti alloy: Low friction coefficient, good bonding and biocompatibility, Materials Science and Engineering: C 71 (2017) 520–528.

[59] M. Li, S. Luo, C. Zeng, J. Shen, H. , others, Corrosion behavior of TiN coated type 316 stainless steel in simulated PEMFC environments, Corrosion science 46 (6) (2004) 1369–1380.

[60] P. Yi, L. Zhu, C. Dong, K. Xiao, Corrosion and interfacial contact resistance of 316L stainless steel coated with magnetron sputtered ZrN and TiN in the simulated cathodic environment of a proton-exchange membrane fuel cell, Surface and Coatings Technology 363 (2019) 198–202.

[61] M. M. Ghorbani, R. Taherian, M. Bozorg, Investigation on physical and electrochemical properties of TiN-coated Monel alloy used for bipolar plates of proton exchange membrane fuel cell, Materials Chemistry and Physics 238 (2019) 121916.

[62] S. Jannat, H. Rashtchi, M. Atapour, M. A. Golozar, H. Elmkhah, M. Zhiani, Preparation and performance of nanometric Ti/TiN multi-layer physical vapor deposited coating on 316L stainless steel as bipolar plate for proton exchange membrane fuel cells, Journal of Power Sources 435 (2019) 226818.

[63] U. DOE, The fuel cell technologies office multi-year research, development, and demonstration plan, Tech. rep., Technical report: US Department of Energy (2016).

[64] Z. Li, K. Feng, Z. Wang, X. Cai, C. Yao, Y. Wu, Investigation of single-layer and multilayer coatings for aluminum bipolar plate in polymer electrolyte membrane fuel cell, International journal of hydrogen energy 39 (16) (2014) 8421–8430.

[65] L. Hultman, Thermal stability of nitride thin films, Vacuum 57 (1) (2000) 1–30.

[66] S. Mahieu, D. Depla, Reactive sputter deposition of TiN layers: modeling the growth by characterization of particle fluxes towards the substrate, Journal of Physics D: Applied Physics 42 (5) (2009) 053002.

[67] F. C. da Silva, M. A. Tunes, P. D. Edmondson, N. B. Lima, J. C. Sagás, L. C. Fontana, C. G. Schön, Grid-assisted magnetron sputtering deposition of nitrogen graded TiN thin films, SN Applied Sciences 2 (5) (2020) 865. doi:10.1007/s42452-020-2617-3.

[68] F. C. Silva, M. A. Tunes, J. C. Sagás, L. C. Fontana, N. B. de Lima, C. G. Schön, Mechanical properties of homogeneous and nitrogen graded tin thin films, Thin Solid Films (2020) 138268.

[69] L. D. Schepper, M. D'Olieslaeger, G. Knuyt, L. Stals, M. V. Stappen], B. Malliet, J. Celis, J. Roos, Initial growth and epitaxy of PVD TiN layers on austenitic steel, Thin Solid Films 173 (2) (1989) 199 – 208. doi:https://doi.org/10.1016/0040-6090(89)90135-1.

[70] C. Quaeyhaegens, L. Stals, M. V. Stappen, L. D. Schepper, Interface study of TiN- and Ti–TiN-coated stainless steel AISI 304 with asymmetric glancing angle X-ray diffraction and classical Bragg-Brentano X-ray diffraction, Thin Solid Films 197 (1) (1991) 37 – 46. doi:https://doi.org/10.1016/0040-6090(91)90219-N.

[71] E. K. Lee, J. K. Kim, T. J. Kim, H. Song, J. H. Kim, S. A. Park, T. G. Jeong, S. W. Yun, J. Lee, J. Goo, J. H. Kim, B. G. Park, H. H. Chun, P. K. Song, C. G. Kang, Y. T. Kim, Enhanced corrosion resistance and fuel cell performance of Al1050 bipolar plate coated with TiN/Ti double layer, Energy Convers. Manag. 75 (2013) 727–733. doi:10.1016/j.enconman.2013.08.041.

[72] L. A. Giannuzzi, F. A. Stevie, A review of focused ion beam milling techniques for tem specimen preparation, Micron 30 (3) (1999) 197–204.

[73] L. Giannuzzi, F. Stevie, A review of focused ion beam milling techniques for TEM specimen preparation, Micron 30 (3) (1999) 197–204. doi:10.1016/S0968-4328(99)00005-0.

[74] A. Young, J. Stumper, E. Gyenge, Characterizing the structural degradation in a PEMFC cathode catalyst layer: carbon corrosion, Journal of The Electrochemical Society 156 (8) (2009) B913–B922.

[75] Y.-H. Yun, Deposition of gold–titanium and gold–nickel coatings on electropolished 316l stainless steel bipolar plates for proton exchange membrane fuel cells, international journal of hydrogen energy 35 (4) (2010) 1713–1718.

[76] C.-H. Lin, S.-Y. Tsai, An investigation of coated aluminium bipolar plates for pemfc, Applied energy 100 (2012) 87–92.

[77] M. Pourbaix, Atlas of electrochemical equilibria in aqueous solution, NACE 307 (1974).

[78] H. Krawiec, V. Vignal, R. Akid, Numerical modelg of the electrochemical behaviour of 316L stainless steel based upon static and dynamic experimental microcapillary-based techniques, Electrochimica acta 53 (16) (2008) 5252–5259.

[79] F. Andreatta, L. Fedrizzi, The use of the electrochemical micro-cell for the investigation of corrosion phenomena, Electrochimica Acta 203 (2016) 337–349.

[80] Basic concepts of the experimental techniques-chapter3, REFUBIUM - FREIE UNIVERSITÄT BERLIN REPOSITORY thesis library orig-basliksiz 28–42.
URL https://refubium.fu-berlin.de/bitstream/handle/fub188/8054/03_chapter3.pdf?sequence=4&isAllowed=y

[81] J. W. Diggle, T. C. Downie, C. Goulding, Anodic oxide films on aluminum, Chemical Reviews 69 (3) (1969) 365–405.

[82] G. Wood, J. O'sullivan, The anodizing of aluminium in sulphate solutions, Electrochimica acta 15 (12) (1970) 1865–1876.

[83] G. Thompson, Porous anodic alumina: fabrication, characterization and applications, Thin solid films 297 (1-2) (1997) 192–201.

[84] W. Lee, S.-J. Park, Porous anodic aluminum oxide: anodization and templated synthesis of functional nanostructures, Chemical reviews 114 (15) (2014) 7487–7556.

[85] X.-F. Zhu, Y. Song, L. Liu, C.-Y. Wang, J. Zheng, H.-B. Jia, X.-L. Wang, Electronic currents and the formation of nanopores in porous anodic alumina, Nanotechnology 20 (2009) 475303.

[86] F. Li, L. Zhang, R. M. Metzger, On the growth of highly ordered pores in anodized aluminum oxide, Chemistry of materials 10 (9) (1998) 2470–2480.

[87] J. R. Mawdsley, J. D. Carter, X. Wang, S. Niyogi, C. Q. Fan, R. Koc, G. Osterhout, Composite-coated aluminum bipolar plates for pem fuel cells, Journal of Power Sources 231 (2013) 106–112.

[88] C.-Y. Bai, Y.-H. Chou, C.-L. Chao, S.-J. Lee, M.-D. Ger, Surface modifications of aluminum alloy 5052 for bipolar plates using an electroless deposition process, Journal of Power Sources 183 (1) (2008) 174–181.

[89] S.-J. Lee, C.-H. Huang, Y.-P. Chen, Investigation of pvd coating on corrosion resistance of metallic bipolar plates in pem fuel cell, Journal of materials processing technology 140 (1-3) (2003) 688–693.

[90] A. E. Fetohi, R. A. Hameed, K. El-Khatib, E. R. Souaya, Ni–p and ni–co–p coated aluminum alloy 5251 substrates as metallic bipolar plates for pem fuel cell applications, international journal of hydrogen energy 37 (9) (2012) 7677–7688.

[91] S.-Y. Tsai, C.-Y. Bai, C.-H. Lin, G.-N. Shi, K.-H. Hou, Y.-M. Liu, M.-D. Ger, The characteristics and performance of electroless nickel and immersion au plated aluminum alloy bipolar plates in polymer electrolyte membrane fuel cells, Journal of Power Sources 214 (2012) 51–58.

[92] S. A. A. El-Enin, O. E. Abdel-Salam, H. El-Abd, A. M. Amin, New electroplated aluminum bipolar plate for pem fuel cell, Journal of Power Sources 177 (1) (2008) 131–136.

[93] C.-H. Lee, Y.-B. Lee, K.-M. Kim, M.-G. Jeong, D.-S. Lim, Electrically conductive polymer composite coating on aluminum for pem fuel cells bipolar plate, Renewable energy 54 (2013) 46–50.

[94] J. Barranco, F. Barreras, A. Lozano, M. Maza, Influence of crn-coating thickness on the corrosion resistance behaviour of aluminium-based bipolar plates, Journal of Power Sources 196 (9) (2011) 4283–4289.

[95] C. M. Brett, On the electrochemical behaviour of aluminium in acidic chloride solution, Corrosion science 33 (2) (1992) 203–210.

[96] F.-H. Cao, Z. Zhang, J.-F. Li, Y.-L. Cheng, J.-Q. Zhang, C.-N. Cao, Exfoliation corrosion of aluminum alloy AA7075 examined by electrochemical impedance spectroscopy, Materials and Corrosion 55 (1) (2004) 18–23.

[97] M. Metikoš-Huković, R. Babić, Z. Grubač, The study of aluminium corrosion in acidic solution with nontoxic inhibitors, Journal of applied electrochemistry 32 (1) (2002) 35–41.

[98] I. V. Aoki, M.-C. Bernard, S. C. De Torresi, C. Deslouis, H. G. de Melo, S. Joiret, B. Tribollet, Ac-impedance and Raman spectroscopy study of the electrochemical behaviour of pure aluminium in citric acid media, Electrochimica acta 46 (12) (2001) 1871–1878.

[99] T. Zhang, W. Jiang, H. Wang, S. Zhang, Synthesis and localized inhibition behaviour of new triazine-methionine corrosion inhibitor in 1 M HCl for 2024-T3 aluminium alloy, Materials Chemistry and Physics 237 (2019) 121866.

[100] J. De Wit, H. Lenderink, Electrochemical impedance spectroscopy as a tool to obtain mechanistic information on the passive behaviour of aluminium, Electrochimica Acta 41 (7-8) (1996) 1111–1119.

[101] J. Bessone, D. Saas, C. Mayer, M. Ebert, W. Lorenz, An EIS study of aluminium barrier-type oxide films formed in different media, Electrochimica Acta 37 (12) (1992) 2283–2290.

[102] F. Marzo, M. Alberro, A. Manso, X. Garikano, C. Alegre, M. Montiel, A. Lozano, F. Barreras, Evaluation of the corrosion resistance of Ni (P) Cr coatings for bipolar plates by electrochemical impedance spectroscopy, International Journal of Hydrogen Energy (2020).

[103] K. Lal, A. Meikap, S. Chattopadhyay, S. Chatterjee, M. Ghosh, K. Baba, R. Hatada, Electrical resistivity of titanium

nitride thin films prepared by ion beam-assisted deposition, Physica B: Condensed Matter 307 (1-4) (2001) 150–157.

[104] M. Popović, M. Novaković, A. Traverse, K. Zhang, N. Bibić, H. Hofsäss, K. Lieb, Modifications of reactively sputtered titanium nitride films by argon and vanadium ion implantation: Microstructural and opto-electric properties, Thin solid films 531 (2013) 189–196.

[105] J. Galván, M. Larrea, I. Braceras, M. Multigner, J. González-Carrasco, In vitro corrosion behaviour of surgical 316LVM stainless steel modified by Si+ ion implantation–An electrochemical impedance spectroscopy study, Journal of Alloys and Compounds 676 (2016) 414–427.

[106] E. Barsoukov, J. R. Macdonald, Impedance spectroscopy theory, experiment, and, Applications, 2nd ed.(Hoboken, NJ: John Wiley &Sons, Inc., 2005) (2005).

[107] A. Lasia, B. Conway, J. Bockris, R. White, Modern aspects of electrochemistry, vol. 32 (1999).

[108] J.-B. Jorcin, M. E. Orazem, N. Pébère, B. Tribollet, Cpe analysis by local electrochemical impedance spectroscopy, Electrochimica Acta 51 (8-9) (2006) 1473–1479.

[109] P. Bonora, F. Deflorian, L. Fedrizzi, Electrochemical impedance spectroscopy as a tool for investigating underpaint corrosion, Electrochimica Acta 41 (7-8) (1996) 1073–1082.

[110] M. E. Orazem, B. Tribollet, Electrochemical impedance spectroscopy, John Wiley & Sons, 2017.

[111] L. S. Barreto, M. S. Tokumoto, I. C. Guedes, H. G. d. Melo, F. Amado, V. R. Capelossi, Study and assessment of the efficiency of the cocoa bark extracted from the theobroma cacao as an inhibitor of the corrosion of carbon steel in substitution of benzotriazole, Materials Research 21 (1) (2018).

[112] P.-g. Sun, C.-Y. Su, T.-P. Liou, C.-H. Hsu, C.-K. , Mechanical behavior of TiN/CrN nano-multilayer thin film deposited by unbalanced magnetron sputter process, Journal of Alloys and Compounds 509 (6) (2011) 3197–3201.

[113] A. Krella, A. Czyzniewski, Influence of the substrate hardness on the cavitation erosion resistance of TiN coating, Wear 263 (1-6) (2007) 395–401.

[114] C.-L. Wang, Y. Gao, G.-T. Bu, G. Shen, Effect of flow ratio of Ar/N (2) on TiN coatings prepared by double glow plasma surface alloying process, Transactions of Materials and Heat Treatment 31 (7) (2010) 119–122.

[115] A. Kumar, D. Singh, R. N. Goyal, D. Kaur, Fabrication and nanoindentation properties of TiN/NiTi thin films and their applications in electrochemical sensing, Talanta 78 (3) (2009) 964–969.

[116] C. Petrogalli, L. Montesano, M. Gelfi, G. La Vecchia, L. Solazzi, Tribological and corrosion behavior of crn coatings: Roles of substrate and deposition defects, Surface and Coatings Technology 258 (2014) 878–885.

[117] J. Creus, H. Idrissi, H. Mazille, F. Sanchette, P. Jacquot, Improvement of the corrosion resistance of crn coated steel by an interlayer, Surface and Coatings Technology 107 (2-3) (1998) 183–190.

[118] M. Song, J. Guo, Y. Yang, K. Geng, M. Xiang, Q. Zhu, C. Hu, H. Zhao, Fe2ti interlayer for improved adhesion strength and corrosion resistance of tin coating on stainless steel 316l, Applied Surface Science 504 (2020) 144483.

[119] J. Vega, H. Scheerer, G. Andersohn, M. Oechsner, Experimental studies of the effect of ti interlayers on the corrosion resistance of tin pvd coatings by using electrochemical methods, Corrosion science 133 (2018) 240–250.

[120] F.-Y. Ouyang, W.-L. Tai, Enhanced corrosion resistance of tin-coated stainless steels for the application in flexible dye-sensitized solar cells, Applied surface science 276 (2013) 563–570.

[121] J.-H. Huang, F.-Y. Ouyang, G.-P. Yu, Effect of film thickness and ti interlayer on the structure and properties of nanocrystalline tin thin films on aisi d2 steel, Surface and Coatings Technology 201 (16-17) (2007) 7043–7053.

[122] B. Chen, W. Pan, G. Yu, J. Hwang, J. Huang, On the corrosion behavior of tin-coated aisi d2 steel, Surface and Coatings Technology 111 (1) (1999) 16–21.

[123] J.-Y. Chen, G.-P. Yu, J.-H. Huang, Corrosion behavior and adhesion of ion-plated tin films on aisi 304 steel, Materials chemistry and physics 65 (3) (2000) 310–315.

[124] Y. Liu, L. Li, X. Cai, Q. Chen, M. Xu, Y. Hu, T.-L. Cheung, C. Shek, P. K. Chu, Effects of pretreatment by ion implantation and interlayer on adhesion between aluminum substrate and tin film, Thin Solid Films 493 (1-2) (2005) 152–159.

[125] L. Shan, Y. Wang, J. Li, H. Li, X. Wu, J. Chen, Tribological behaviours of pvd tin and ticn coatings in artificial seawater, Surface and Coatings Technology 226 (2013) 40–50.

[126] J. A. Thornton, Influence of apparatus geometry and deposition conditions on the structure and topography of thick sputtered coatings, Journal of Vacuum Science and Technology 11 (4) (1974) 666–670.

[127] R. Messier, A. Giri, R. Roy, Revised structure zone model for thin film physical structure, Journal of Vacuum Science & Technology A: Vacuum, Surfaces, and Films 2 (2) (1984) 500–503.

[128] J. A. Thornton, D. Hoffman, Stress-related effects in thin films, Thin solid films 171 (1) (1989) 5–31.

[129] S. Mahieu, P. Ghekiere, D. Depla, R. De Gryse, Biaxial alignment in sputter deposited thin films, Thin Solid Films 515 (2006) 1229–1249. doi:10.1016/j.tsf.2006.06.027.

[130] M. Larijani, M. Elmi, M. Yari, M. Ghoranneviss, P. Balashabadi, A. Shokouhy, Nitrogen effect on corrosion resistance of ion beam sputtered nanocrystale zirconium nitride films, Surface & coatings technology 209 (2009) 2591–2594.

[131] R. Egerton, Eels in the electron microscope, Springer, New York) p 226 (1986).

[132] R. Feynman, et al., The Feynman Lectures on Physics: volume two, Addison-Wesley, Reading, 1977.

[133] R. Brydson, Electron Energy Loss Spectroscopy, BIOS Scientific Publishers Ltd, Oxford, United Kingdom, 2001.

[134] F. Roth, A. König, J. Fink, B. Büchner, M. Knupfer, Electron energy-loss spectroscopy: A versatile tool for the investigations of plasmonic excitations, Journal of Electron Spectroscopy and Related Phenomena 195 (2014) 85–95. arXiv:arXiv:1405.3369v1, doi:10.1016/j.elspec.2014.05.007.

[135] M. A. Tunes, C. M. Silva, P. D. Edmondson, Site specific dependencies of hydrogen concentrations in zirconium hydrides, Scripta Materialia 158 (2019) 136–140.

[136] C. C. Ahn, Transmission electron energy loss spectrometry in materials science and the EELS atlas, John Wiley & Sons, 2006.

[137] C. Colliex, Electron energy loss spectroscopy in the electron microscope, Academic Press, 1984.